A&A 670, A9 (2023)
https://doi.org/10.1051/0004-6361/202143019

Astronomy & Astrophysics

A global view on star formation: The GLOSTAR Galactic plane survey

VI. Radio Source Catalog II: 28° < ℓ < 36° and |b| < 1°, VLA B-configuration★

S. A. Dzib[1,2], A. Y. Yang[2], J. S. Urquhart[3], S.-N. X. Medina[2,4], A. Brunthaler[2], K. M. Menten[2], F. Wyrowski[2], W. D. Cotton[5], R. Dokara[2], G. N. Ortiz-León[2,6], M. R. Rugel[2], H. Nguyen[2], Y. Gong[2], A. Chakraborty[7], H. Beuther[8], S. J. Billington[3], C. Carrasco-Gonzalez[9], T. Csengeri[10], P. Hofner[5,11], J. Ott[4], J. D. Pandian[12], N. Roy[13], and V. Yanza[9]

[1] IRAM, 300 rue de la piscine, 38406 Saint-Martin-d'Hères, France
[2] Max-Planck-Institut für Radioastronomie (MPIfR), Auf dem Hügel 69, 53121 Bonn, Germany
e-mail: sdzib@mpifr-bonn.mpg.de
[3] Centre for Astrophysics and Planetary Science, University of Kent, Canterbury, CT2 7NH, UK
[4] German Aerospace Center, Scientific Information, 51147 Cologne, Germany
[5] National Radio Astronomy Observatory, 520 Edgemont Road, Charlottesville, VA 22903, USA
[6] Instituto de Astronomía, Universidad Nacional Autónoma de México (UNAM), Apdo Postal 70-264, México, D.F., Mexico
[7] McGill University, 3600 rue University, Montreal, QC H3A 2T8, Canada
[8] Max Planck Institute for Astronomy, Koenigstuhl 17, 69117 Heidelberg, Germany
[9] Instituto de Radioastronomía y Astrofísica (IRyA), Universidad Nacional Autónoma de México Morelia, 58089 México, Mexico
[10] Laboratoire d'astrophysique de Bordeaux, Univ. Bordeaux, CNRS, B18N, allée Geoffroy Saint-Hilaire, 33615 Pessac, France
[11] Physics Department, New Mexico Tech, 801 Leroy Place, Socorro, NM 87801, USA
[12] Department of Earth and Space Science, Indian Institute for Space Science and Tecnology, Trivandrum 695547, India
[13] Department of Physics, Indian Institute of Science, Bangalore 560012, India

Received 30 December 2021 / Accepted 28 September 2022

ABSTRACT

As part of the Global View on Star Formation (GLOSTAR) survey we have used the *Karl G. Jansky* Very Large Array (VLA) in its B-configuration to observe the part of the Galactic plane between longitudes of 28° and 36° and latitudes from −1° to +1° at the *C*-band (4–8 GHz). To reduce the contamination of extended sources that are not well recovered by our coverage of the (u, v)-plane, we discarded short baselines that are sensitive to emission on angular scales >4″. The resulting radio continuum images have an angular resolution of 1.″0 and a sensitivity of ∼60 μJy beam^{-1}, making it the most sensitive radio survey covering a large area of the Galactic plane with this angular resolution. An automatic source extraction algorithm was used in combination with visual inspection to identify a total of 3325 radio sources. A total of 1457 radio sources are ≥7σ and comprise our highly reliable catalog; 72 of these are grouped as 22 fragmented sources, for example, multiple components of an extended and resolved source To explore the nature of the cataloged radio sources, we searched for counterparts at millimeter and infrared wavelengths. Our classification attempts resulted in 93 H II region candidates, 104 radio stars, and 64 planetary nebulae, while it is suggested that most of the remaining radio sources are extragalactic sources. We investigated the spectral indices (α, $S_\nu \propto \nu^\alpha$) of radio sources classified as H II region candidates and found that many have negative values. This may imply that these radio sources represent young stellar objects that are members of the star clusters around the high-mass stars that excite the H II regions, but not these H II regions themselves. By comparing the peak flux densities from the GLOSTAR and CORNISH surveys, we have identified 49 variable radio sources, most of them with an unknown nature. Additionally, we provide a list of 1866 radio sources detected within 5 to 7σ levels.

Key words. catalogs – surveys – radio continuum: general – stars: formation – techniques: interferometric

1. Introduction

The Global View on Star Formation (GLOSTAR) survey is presently the most sensitive radio survey (∼60 μJy beam^{-1}) of the northern hemisphere of the Galactic plane at the *C*-band (4–8 GHz) (Brunthaler et al. 2021; Medina et al. 2019). Making full use of the capabilities of the *Karl G. Jansky* Very Large Array (VLA), a distinction of GLOSTAR compared to previous surveys is that it simultaneously observes radio continuum and spectral line emission. The GLOSTAR survey is indeed complementary to the wealth of Galactic plane surveys at infrared and submillimeter wavelengths that address star formation in the Galaxy, some of which are described in Sect. 3.7.

The primary goal of the GLOSTAR survey is to localize signposts of massive star formation (MSF) activity (see Brunthaler et al. 2021, for a detailed overview of the survey). Toward this goal, in the continuum mode, the survey mainly observes compact, ultracompact, and hypercompact HII regions that trace different early phases of MSF activity (e.g.,

★ Full Tables 1 and A.1 are only available at the CDS via anonymous ftp to cdsarc.cds.unistra.fr (130.79.128.5) or via https://cdsarc.cds.unistra.fr/viz-bin/cat/J/A+A/670/A9

Medina et al. 2019; Nguyen et al. 2021). Thus, the GLOSTAR survey complements previous radio surveys by providing a powerful and comprehensive radio-wavelength survey of the ionized gas in the Galactic plane with an unprecedented sensitivity. However, the survey area is also populated with radio sources related to post-main-sequence stars (e.g., Wolf–Rayet stars, pulsars), planetary nebulae, supernova remnants, and extragalactic radio sources (Medina et al. 2019; Chakraborty et al. 2020; Dokara et al. 2021). In spectral line mode, it traces the radio recombination lines from regions ionized by massive stars and the methanol maser line at 6.7 GHz (Ortiz-León et al. 2021; Nguyen et al. 2022), both of which are related to MSF. The formaldehyde absorption line at 4.8 GHz is also observed. It traces neutral molecular gas and its radial velocity information with respect to the local standard of rest (LSR) radial can help to solve distance ambiguities. The final GLOSTAR images will cover the Galactic plane between Galactic longitudes, ℓ, of -2° and 60°, latitudes, b, from -1° to $+1^\circ$, and the Cygnus X region. The final data set will consist of low-resolution images ($\sim$20″) using the VLA in the D-configuration and high-resolution images ($\sim$1.″0) using the B-configuration. These VLA data sets could also be combined for optimal sensitivity of the intermediate spatial ranges, and such images will be presented in future works. The VLA observations will be complemented with very low-resolution ($\sim$150″) images of single-dish observations from the Effelsberg radio telescope, to recover the most extended emission and solve the "missing short spacing" issue affecting interferometer-only images. The overview of the full GLOSTAR capabilities are described in detail by Brunthaler et al. (2021).

Previously, we have reported the radio source catalog of the low-resolution VLA images covering the area $28^\circ < \ell < 36^\circ$ and $-1^\circ < b < +1^\circ$ (Medina et al. 2019). Complementary infrared- and submillimeter-wavelength data were examined toward the radio source positions with the goal of elucidating the nature of the radio sources. In this paper we report the compact ($\sim$1.″0) radio sources from the same region using the high-resolution observations obtained with the VLA in B-configuration. The particularity of this new catalog is that we can identify the most compact, and probably youngest, (hypercompact) HII regions.

2. Observations

The VLA of the National Radio Astronomy Observatory[1] was used in its B-configuration to observe the (4–8 GHz) continuum emission. We followed the same instrumental setups and calibration as for the D-configuration data. We refer the reader to the overview paper (Brunthaler et al. 2021) for a detailed description of the data management that we summarize in the following subsections.

2.1. Observation strategy

The correlator setup consisted of two 1-GHz-wide sub-bands, centered at 4.7 and 6.9 GHz. Each sub-band was divided into eight spectral windows of 128 MHz, and each spectral window comprised 64 channels with a channel width of 2 MHz[2]. The chosen setup prevented strong persistent radio frequency interference (RFI) seen (most prominently) at 6.3 and 4.1 GHz, and it enabled the estimation of source spectral indices.

For each epoch the total observing time was 5 h. At the beginning of the observations, the amplitude/bandpass calibrator 3C 286 was observed for 10 min. Then, the phase calibrator, J1804+0101, was observed for 1 min, followed by pointings on target fields for 8 min, after which the phase calibrator was observed for another minute. The observation cycle, consisting of phase calibrator–targets scans, was repeated over the full 5 h. During this time, an area of $2^\circ \times 1^\circ$ was covered with phase centers for 676 target fields in a semi-mosaic mode (see Brunthaler et al. 2021, for a detailed overview of the observation strategy). Each pointing was observed twice for 11 s, which, after considering the slewing time, yielded a total integration time of 15 s per field. The theoretical noise level in brightness (or peak flux density) from these observations was 90 μJy beam^{-1} per field and per sub-band. The noise was improved after combining the fields and both sub-bands by a factor of roughly two. We observed a total of eight epochs, or a total of 40 h of telescope time, under project ID VLA/13A-334. The total covered area was 16 square degrees. The observations were taken during the period from 2013 September to 2014 January.

2.2. Calibration, data reduction, and imaging

The data were calibrated, edited and imaged using the *Obit* software environment (Cotton 2008), which interoperates with the classic Astronomical Image Processing Software (AIPS) package (Greisen 2003). We have written calibration scripts that handle the GLOSTAR data edition and calibration (Brunthaler et al. 2021). The calibration follows the standard procedures of editing and calibrating interferometric data. These include bandpass, amplitude, and phase calibration.

The calibrated data were imaged using the Obit task MFImage. The CLEANing process from MFImage divides the observed band into nine frequency bins that are narrow enough to perform a spectral deconvolution, addressing the effects of variable spectral index and antenna pattern variations. In the end, we obtained an image representing the data for the full frequency band and images of each individual frequency bin. The images were obtained from the data that had projected baselines with distances in the (u, v)-plane larger than 50 kλ; in other words, they were obtained by discarding all radio emission on angular scales larger than $\approx$4.″13 at all observed frequencies. This choice rejected emission from poorly mapped extended structures that introduced artifacts in the images, with a minor impact on the overall sensitivity. The images were convolved with a circular beam of size 1.″0 and with a pixel size of 0.″25. The mosaics were constructed to obtain images of 35 000 × 30 000 pixels, containing the $1^\circ \times 2^\circ$ angular area surveyed by epoch, following the schemes described by Brunthaler et al. (2021). The mean measured noise in the resulting images was 60 μJy beam^{-1}, although it could be significantly higher in some areas in which extended emission was not properly recovered or around very bright radio sources that produce imperfectly cleaned sidelobe emission.

3. Catalog construction

In this section, we discuss the procedure used for constructing the catalogs presented in this work. First, we extracted the sources from the images, selected the sources that are real, identified candidate radio sources, and discarded image artifacts. We

[1] The National Radio Astronomy Observatory is a facility of the National Science Foundation operated under cooperative agreement by Associated Universities, Inc.

[2] Higher-frequency resolution correlator windows were used to cover the prominent methanol maser emission line at 6.7 GHz, formaldehyde absorption at 4.8 GHz, and seven radio recombination lines. The full results of these line observations will be reported in forthcoming papers.

Table 1. GLOSTAR B-configuration catalog for 28° < ℓ < 36° and |b| < 1°.

GLOSTAR B-conf. name	ℓ	b	S/N	S_{peak}	$\sigma_{S_{peak}}$	S_{int}	$\sigma_{S_{int}}$	Y	R_{eff}	α	GLOSTAR D-conf. name	Infrared counterpart			Submillimeter counterpart	Classification
				(mJy beam^{-1})		(mJy)			(″)			NIR	MIR	FIR		
(1)	(2)	(3)	(4)	(5)	(6)	(7)	(8)	(9)	(10)	(11)	(12)	(13)	(14)	(15)	(16)	(17)
G028.0014+00.0567	28.00144	+0.05670	15.6	0.90	0.08	0.86	0.07	0.95	0.8	+0.28 ± 0.24	G028.002+00.057					EgC
G028.0050+00.1497	28.00503	+0.14967	10.2	0.60	0.07	0.66	0.07	1.09	0.7	−0.50 ± 0.60	G028.005+00.150					EgC
G028.0065–00.9904	28.00648	–0.99038	35.6	2.49	0.15	2.48	0.14	1.00	0.9	−0.24 ± 0.06	G028.007–00.990	✓				EgC
G028.0101–00.3032	28.01014	–0.30323	12.6	0.69	0.07	0.72	0.07	1.04	0.8	−0.11 ± 0.36	G028.010–00.303					EgC
G028.0239+00.5132	28.02391	+0.51318	13.8	0.92	0.08	0.97	0.08	1.05	0.8	+0.34 ± 0.35	G028.024+00.514					EgC
G028.0309+00.6677	28.03085	+0.66769	08.2	0.54	0.07	0.62	0.07	1.13	0.7	...	G028.031+00.669		✓			EgC
G028.0314–00.0726	28.03136	–0.07260	31.9	2.03	0.13	2.44	0.14	1.20	1.0	−0.79 ± 0.14	...					EgC
G028.0350+00.3898	28.03495	+0.38978	10.2	0.69	0.08	0.70	0.08	1.01	0.7	−0.59 ± 0.37	...					EgC
G028.0403–00.2452	28.04027	–0.24519	09.2	0.56	0.07	0.52	0.07	0.94	0.7	...	...					EgC
G028.0474–00.9892	28.04741	–0.98918	23.2	1.86	0.13	2.10	0.13	1.13	0.9	−0.33 ± 0.25	G028.048–00.989					EgC
G028.0489–00.8699	28.04894	–0.86986	16.2	1.03	0.08	1.05	0.08	1.02	0.8	+0.45 ± 0.25	G028.049–00.869					EgC
G028.0594+00.1197	28.05937	+0.11975	11.5	0.84	0.09	0.84	0.08	1.00	0.7	+0.36 ± 0.46	G028.065+00.119					EgC
G028.0654+00.1184	28.06544	+0.11842	25.1	1.77	0.12	2.01	0.12	1.14	1.0	−0.71 ± 0.26	...					EgC
G028.0749–00.2953	28.07494	–0.29530	19.1	1.28	0.10	1.42	0.10	1.11	0.9	−0.88 ± 0.27	G028.075–00.296	✓				EgC
G028.0850–00.5583	28.08501	–0.55826	28.4	1.69	0.11	1.76	0.11	1.04	0.9	−0.34 ± 0.16	G028.085–00.558	✓				EgC

Notes. Only a small portion of the data is provided here. The full table is available in electronic form at the CDS. Classification (17) see also Sect. 3.8: EgC = extragalctic radio source candidate, HII = HII region candidate, Radio star, PN = planetary nebula, WR = Wolf–Rayet star, PDR = photodissociation region, Cataclysmic variable, Pulsar, and Unclear = source with no clear classification.

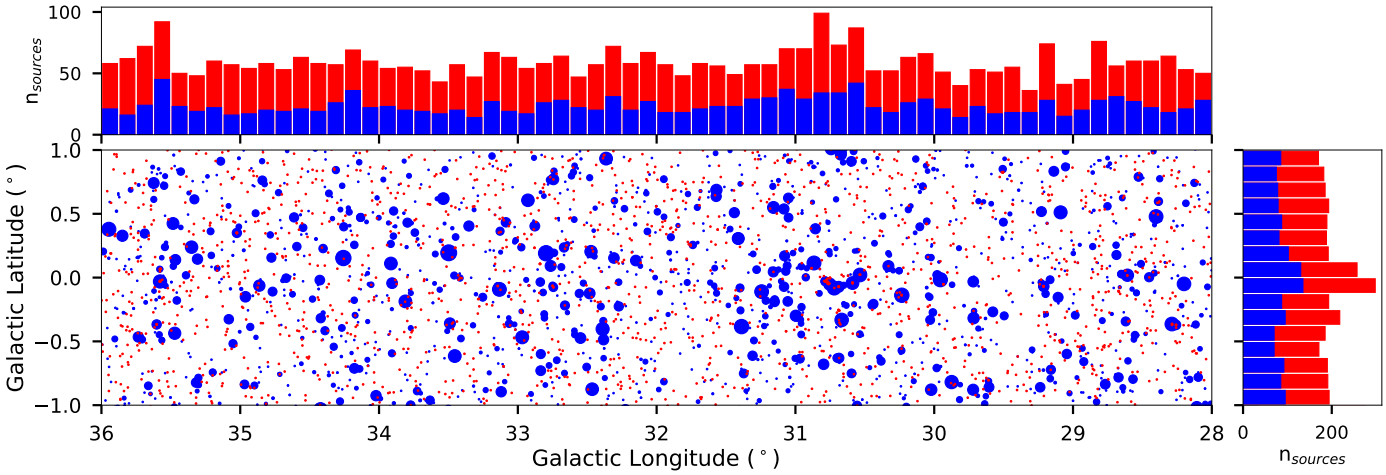

Fig. 1. Spatial distribution of sources extracted from the VLA B-configuration images. Blue circles indicate the positions of highly reliable sources. Their sizes are scaled (nonlinearly) with the flux intensity. Red points indicate the position of sources with 5–7σ levels. The *top* and *right panels* are the histograms of the source distributions in the Galactic longitude and Galactic latitude, respectively.

investigated the astrometry, flux density (S_ν), spectral indices (α; $S_\nu \propto \nu^\alpha$), and searched for counterparts at other wavelengths. Based on the counterpart information, we attempted a classification of the radio sources. The final catalog is presented in Table 1, with the reliable radio sources, their properties, and the source classification.

3.1. Source extraction

The source extraction was performed following the procedures described by Medina et al. (2019), and we refer the reader to that work for the details, while here we give a brief summary. Using the SExtractor (Bertin & Arnouts 1996) tool from the Graphical Astronomy and Image Analysis Tool package (*Gaia*[3]), we first created a noise image. Then, we used the BLOBCAT package (Hales et al. 2012) to extract the sources from each of the final images. Both the intensity map and the noise map were used as inputs by BLOBCAT. This package recognizes islands of pixels (blobs) representing sources with a minimum peak flux above N times the noise level in the area. Purcell et al. (2013) noted that with $N < 4.5$, large radio images will be dominated by spurious sources. Thus, to diminish the number of spurious detections in our catalog, for our extraction we initially defined $N = 5$ and required blobs to consist of a minimum of 12 contiguous pixels. The minimum number of pixels was chosen to be the number of expected pixels in 50% of the beam area. The final number of extracted blobs was 3880. After this first extraction, we performed a visual inspection of all the blobs to identify clear image artifacts, such as sidelobes from very bright radio sources, and discarded 555 blobs. The spatial distribution of all the blobs, excluding the artifacts, is shown in Fig. 1. We detected a total of 1457 blobs with a signal-to-noise ratio (S/N) ≥ 7.0 and 1866 blobs with 5.0 ≤ S/N < 7.0.

It has been determined that in large radio surveys such as GLOSTAR, the most reliable sources are those with peak flux

[3] http://starlink.rl.ac.uk/star/docs/sun214.htx/sun214.html

values above $7\sigma_{\rm noise}$ as no spurious sources are expected at these levels (e.g., Purcell et al. 2013; Bihr et al. 2016; Wang et al. 2018; Medina et al. 2019). However, as some blobs with a brightness between 5–$7\sigma_{\rm noise}$ could represent real sources, we searched for counterparts inside a radius of 2″ in the SIMBAD astronomical database[4] for all sources (see details below). This comprehensive database is the best option to look for counterparts at any wavelength in large areas of the sky but, admittedly, it can miss recent catalogs. We also considered weak blobs (peak flux values <$7\sigma_{\rm noise}$) as real radio sources whose positions are consistent with the radio sources from our D-configuration catalog by Medina et al. (2019). The full number of weak blobs with a known counterpart in the SIMBAD database and our D-configuration catalog is 142. The remaining 1724 radio blobs having a S/N between 5 and 7, and having no known counterpart, are referred to as candidate radio source detections. We give the list of these 1866 sources with a $S/N < 7$ in Table A.1, labeling those with SIMBAD or D-configuration counterparts, and we do not analyze them further.

We consider the remaining 1457 blobs as highly reliable radio sources. They are represented by the blue circles in Fig. 1 and are listed in Table 1. The position, the S/N, the peak, and the integrated flux density values (Cols. 2–8 in Table 1) are taken from the values determined by the BLOBCAT software (Hales et al. 2012). From now on, this paper will focus on the analysis of these sources. Considering the ratio between the integrated flux density (in units of Jy) and the peak flux density (in units of Jy beam^{-1} (here named as the Y-factor; $Y = S_{\nu,\rm Int}/S_{\nu,\rm Peak}$) we can divide these sources into extended ($Y > 2.0$), compact ($1.1 < Y \leq 2.0$) and point-like ($Y \leq 1.1$) sources. The Y-factor of each source is listed in Col. 9 of Table 1. Using this classification we obtained 100 extended, 455 compact, and 904 point-like sources. As expected for these images, the sources are dominated by compact and point-like sources, as we rejected extended structures in our imaging process.

3.2. Astrometry

For our previous catalog based on the VLA D-configuration observations, we estimated that the accuracy of the astrometry was on the order of 1″. The position errors of the extracted sources with BLOBCAT in the VLA B-configuration images have a mean value of 0.″06 in both Galactic longitude and latitude. The 0.″06 is a formal statistical error estimate from BLOBCAT and does not reflect position errors resulting from imperfect phase calibration. As most of the observed radio sources are expected to be background extragalactic objects, the proper motion of these sources is expected to be zero. The only other recent Galactic plane survey that observed the same region at a similar radio frequency is the Co-Ordinated Radio 'N' Infrared Survey for High-mass star formation (CORNISH; Hoare et al. 2012; Purcell et al. 2013). The observations of CORNISH were obtained at 5 GHz using the VLA in its B-configuration. Because of the similarity of the frequency and the use of the same VLA array configuration, the angular resolution of CORNISH is 1.″5, similar to that of the GLOSTAR survey B array data discussed here (1.″0).

A total of 257 compact and point-like sources are listed in both the GLOSTAR-B and CORNISH catalogs (Purcell et al. 2013) with a maximum angular separation of 1.″5, the CORNISH angular resolution. In the upper panel of Fig. 2, the measured offsets of these sources are plotted. We obtained mean and standard

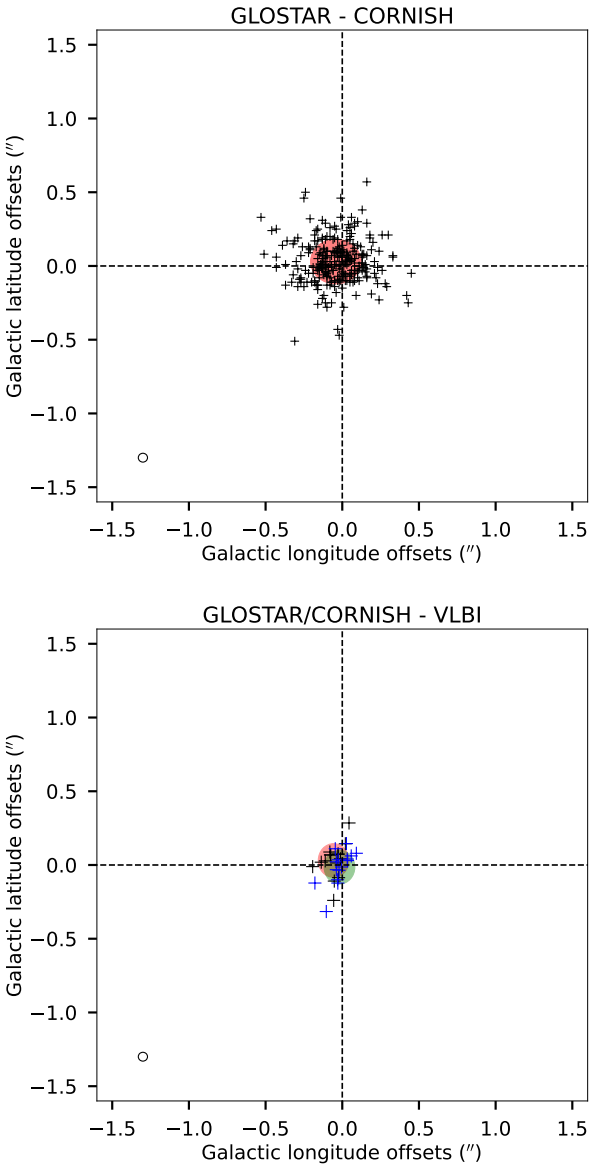

Fig. 2. Comparison of GLOSTAR astrometry with CORNISH and VLBI results. *Upper panel*: position offsets between GLOSTAR compact and point-like sources ($Y \leq 2$) and CORNISH sources. The filled red ellipse is centered in the mean values of the offsets and the size of the semiaxes are equal to the standard deviations. *Lower panel*: same as for the top panel, but for position offsets of GLOSTAR (black crosses, red filled ellipse) and CORNISH (blue crosses, green filled ellipse) sources between the measured positions and the VLBI positions. Open black circles in the bottom left of both panels indicate the mean of position errors of GLOSTAR-B sources.

deviation for the position offsets of $-0.''04 \pm 0.''01$ and 0.″17 in the Galactic longitude direction, and $0.''03 \pm 0.''01$ and 0.″15 in the Galactic latitude direction. The mean offsets in both directions are smaller than the mean position error of GLOSTAR radio sources, suggesting a good astrometry.

The most accurate positions of radio sources were obtained using the Very Long Baseline Interferometry (VLBI) technique. The Radio Fundamental catalog of extragalactic radio sources compiles the positions of ∼19 000 sources that have been measured with VLBI[5]. In this catalog we found 15 sources

[4] http://simbad.u-strasbg.fr/simbad/

[5] The full Radio Fundamental catalog can be accessed via the webpage http://astrogeo.org/

detected both by GLOSTAR and CORNISH. In the lower panel of Fig. 2, we show the offsets between the GLOSTAR and the VLBI positions as black crosses, and the offsets between the CORNISH and VLBI positions as blue crosses. The mean GLOSTAR−VLBI position offset and its standard deviation are −0.″05 ± 0.″02 and 0.″06, respectively, in the Galactic longitude direction, and 0.″03 ± 0.″03 and 0.″11, respectively, in the Galactic latitude direction. On the other hand, the mean CORNISH−VLBI position offset and its standard deviation are −0.″02 ± 0.″02 and 0.″07, respectively, in the Galactic longitude direction, and −0.″02 ± 0.″03 and 0.″10, respectively, in the Galactic latitude direction. The conclusion from this analysis is that the astrometry of the B-configuration GLOSTAR images presented in this paper is accurate to better than 0.″1.

3.3. Comparison with the D-configuration catalog

In the first GLOSTAR catalog, we reported a total of 1575 discrete sources detected in the same region presented in this paper, but based on data obtained with the VLA in its most compact (D) configuration. The GLOSTAR images from the VLA D-configuration observations have an angular resolution of 18″, that is, 18 times larger than the VLA B-configuration images presented in this paper, which also excluded the shortest baselines to further filter out extended emission, resulting in some expected differences. First, given the higher angular resolution observations of the B-configuration, the extended radio sources reported by Medina et al. (2019) were resolved out and, in some cases, only the brightest peaks of extended sources were detected. It is worth noting that some compact sources detected in the B-configuration images can be seen projected on the area of the extended sources, although they do not represent their direct counterpart. Their possible relation must be studied further in the future (e.g., upper panel of Fig. 3). Second, some multiple component radio sources that were unresolved or slightly resolved in the D-configuration images will be resolved in the B-configuration images (middle-panel of Fig. 3) and the integrated flux densities of the individual components can be estimated. Third, some individual radio sources detected in the D-configuration images can be resolved and appear as fragmented radio sources in the B-configuration images (lower panel of Fig. 3). In total, we have found that 95 sources in the D-configuration images are resolved into 224 B-configuration sources (see Col. 12 of Table 1).

The components of fragmented radio sources are grouped and treated as a single source. However, the information of each single component is given in Table 1 and the fragmented sources are listed in Table 2. The integrated flux density reported in Table 2 was obtained by adding the integrated flux densities of the individual fragments. In total, 72 sources recovered from `BLOBCAT` are grouped into 22 fragmented sources.

Other sources were detected as single compact sources in both D- and B-configuration images, and can be considered as direct counterparts. The mean position error of D-configuration sources was 1.″2 (Medina et al. 2019) and the beam size of the B-configuration images was 1.″0. Thus, by adding these values in quadrature, we used a maximum angular separation of 2″ between sources in both catalogs to consider them as direct counterparts. The number of matching sources between both catalogs with this criterion is 372. A further 312 matching sources were found using an angular separation of 9″, half of the angular resolution of the D-configuration images, for which the association must be investigated further. Given the differences described

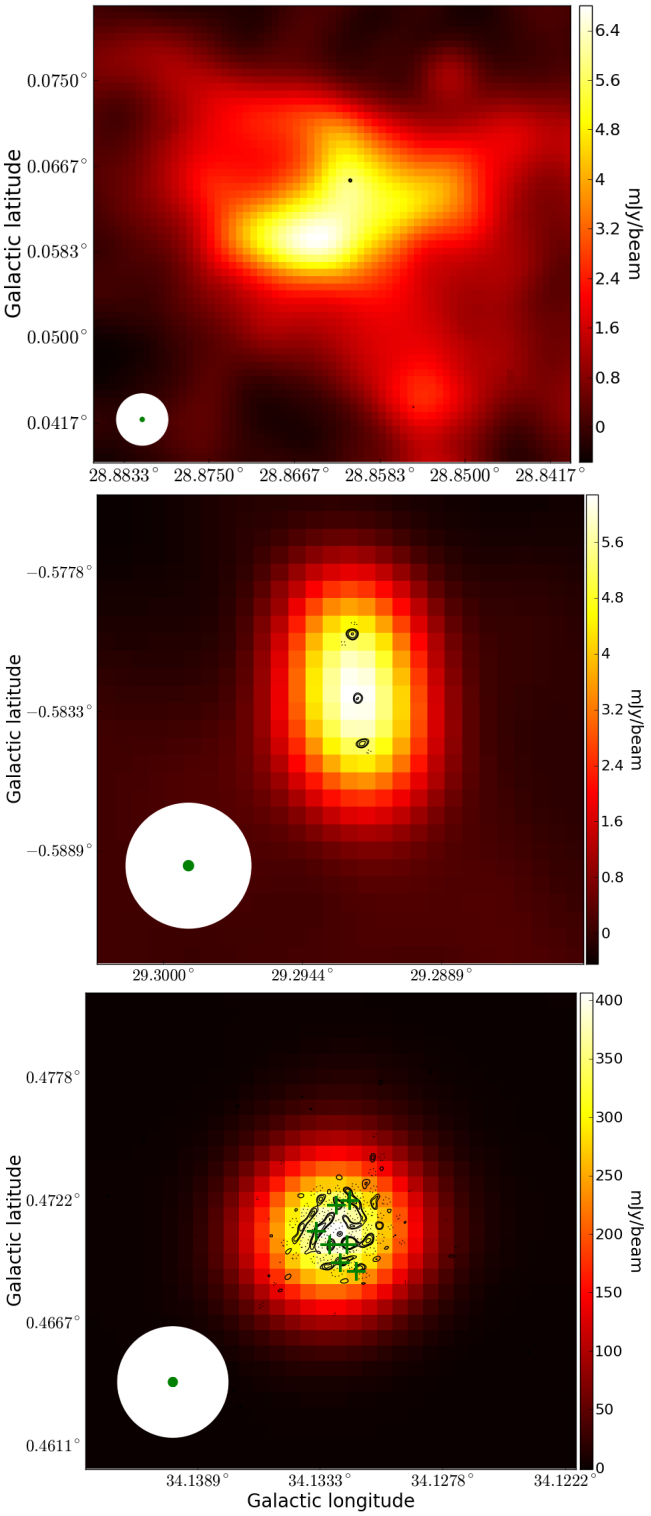

Fig. 3. Source examples of the differences between the two sets of VLA images, D-configuration (background), and B-configuration (contours). The contour levels are –5.0, 5.0, 7.0, 10.0, and 15.0 times the 60 μJy beam^{-1}, the mean noise level of the images. The circles at the bottom left side indicate the beam sizes of the D-configuration (18″, white) and B-configuration (1.″5, green) images. *Top*: B-configuration compact radio source seen in projection in the area of a D-configuration extended radio source. *Middle*: D-configuration compact source that is resolved in three individual compact radio sources in the B-configuration images. *Bottom*: D-configuration compact source that is resolved as a fragmented radio source. The position of fragments considered in the final catalog are indicated with green crosses.

Table 2. GLOSTAR D-configuration sources that are detected as fragmented sources (e.g., multiple components of an extended and resolved source) in the B-configuration images.

GLOSTAR B-conf. name (1)	GLOSTAR D-conf. name (2)	# frag. (3)	$S_{\rm int}$ (mJy) (4)	Class (5)
G028.2440+000.0143	G028.245+00.013	2	01.73	HII
G028.4518+000.0029	G028.451+00.003	3	12.98	HII
G028.6520+000.0278	G028.652+00.027	3	12.23	HII
G028.6871+000.1771	G028.688+00.177	2	10.48	HII
G029.9558–000.0167	W43 south-center	5	375.51	HII
G030.2529+000.0538	G030.253+00.053	3	06.31	HII
G030.9582+000.0868	G030.955+00.081	3	06.61	HII
G031.0695+000.0506	G031.069+00.050	2	09.11	HII
G031.2435–000.1103	G031.243–00.110	4	184.42	HII
G031.2797+000.0623	G031.279+00.063	4	10.15	HII
G031.4118+000.3064	G031.412+00.307	3	84.14	HII
G032.1501+000.1335	G032.151+00.133	5	27.41	HII
G032.2726–000.2257	G032.272–00.226	3	12.81	HII
G032.7965+000.1909	G032.798+00.191	2	574.36	HII
G032.9272+000.6060	G032.928+00.606	2	71.99	HII
G033.9145+000.1104	G033.914+00.110	3	106.65	HII
G034.1321+000.4720	G034.133+00.471	8	23.45	HII
G034.2571+000.1533	G034.260+00.125	3	733.11	HII
G034.8624–000.0630	G034.862–00.063	2	34.16	PN
G035.0521–000.5178	G035.052–00.518	2	08.62	HII
G035.4666+000.1393	G035.467+00.139	2	35.17	HII
G035.5641–000.4909	G035.564–00.492	4	07.93	PN

Notes. Col. 1 gives the name of the brightest fragment.

above, the matching of sources between both catalogs is not expected to be one-to-one.

In Col. 12 of Table 1, we list the GLOSTAR D-configuration name to the B-configuration source with which it is related. With the D-configuration name, we have also labeled the sources that are related to two or more B-configuration sources and if they are considered as individual (I) or fragmented (F) sources. In total, 908 B-configuration sources were related to 780 D-configuration sources. The remaining 551 B-configuration sources have no counterpart in the D-configuration catalog. Most of these sources are located in the inner parts of the Galactic plane (see Fig. 4) where the noise level is higher in the D-configuration images because of the bright and extended radio sources (see the lower panel of Fig. 1 in Medina et al. 2019). As the noise levels could be as high as 500 μJy beam^{-1}, it explains why most of the sources were not detected in the D-configuration images, but were detected in the B-configuration images where the noise level is about ten times lower.

3.4. Source sizes

The source sizes were obtained following Medina et al. (2019), who determined the source effective radius. `BLOBCAT` determined the number of pixels comprising each source, which can be used to estimate the area (A) covered by the source using the pixel size of $0\farcs25 \times 0\farcs25$. Then the effective radius can be determined using

$$R_{\rm eff} = \sqrt{\frac{A}{\pi}}.$$

The effective radius distribution is shown in Fig. 5, and the value for each source is listed in Col. 10 of Table 1.

3.5. Flux densities

To estimate the reliability of the radio source flux densities determined from the GLOSTAR images, we compared the results from the `BLOBCAT` extraction with those in the CORNISH catalog. As most of the sources are expected to be extragalactic sources whose variability is expected to be low (typically only a few percent over timescales of several years), these provide a good point of comparison. We compared sources that are point-like, and thus used the peak flux density. Moreover, we only compared sources whose peak flux densities were above 2.7 mJy in both catalogs, as this is the 7σ base point in the high-reliability source catalog of CORNISH (Purcell et al. 2013). We found 207 sources that meet these criteria. A difference between both catalogs is the mean observed frequency. CORNISH observed at 5 GHz, and GLOSTAR observed a wider bandwidth centered at 5.8 GHz. Thus, the measured flux density is expected to differ slightly for this observational mismatch due to the spectral index. Assuming that the extragalactic objects have a mean spectral index of −0.7 (Condon 1984), the CORNISH flux values will be on average 10% higher than in GLOSTAR.

In the upper panel of Fig. 6, we plot the peak flux densities measured by the CORNISH survey as a function of the peak flux densities measured in this work. The dashed line indicates the equality line and most of the sources are around this line. The lower panel of this figure shows the distribution of the peak flux density ratio between the results from both catalogs. A Gaussian fit to the distribution indicates that the mean value is 1.11 ± 0.03 with a standard deviation of 1.28. Considering the expected higher values in the CORNISH catalog, we conclude that the integrated and peak flux densities of the GLOSTAR-B radio sources are accurate to within 10%.

3.6. Spectral indices

The spectral index of a radio source gives us information on the dominant emission mechanism. Using the wide frequency coverage of our observations, we can estimate the spectral index within the observed band. We measured the peak flux density in each of the imaged frequency bins for compact and point-like sources that have $S/N > 10$ in our main source extraction, a total of 988 sources. The constraint of the S/N was chosen to consider that the noise level in each of the imaged frequency bins will be ∼3× higher, and thus may not be detected in the individual frequency bin images, or their determined values will be affected by noise. On the other hand, over the area covered by an extended source, flux density variations that will depend on its structure may be observed at each frequency, and are thus not considered for this analysis. To obtain the spectral index, we assumed that in the observed frequency range, the flux density is described by the linear equation:

$$\log S_\nu = \alpha \cdot \log \nu + C.$$

A weighted least-square fitting was made to the measured flux densities. Independent spectral index values for each source are listed in Col. 11 in Table 1. The distribution of the determined spectral indices is shown in Fig. 7. The distribution of spectral indices has a mean value of -0.66 ± 0.02.

Spectral indices at radio frequencies in the same area of the presented images were measured previously in the

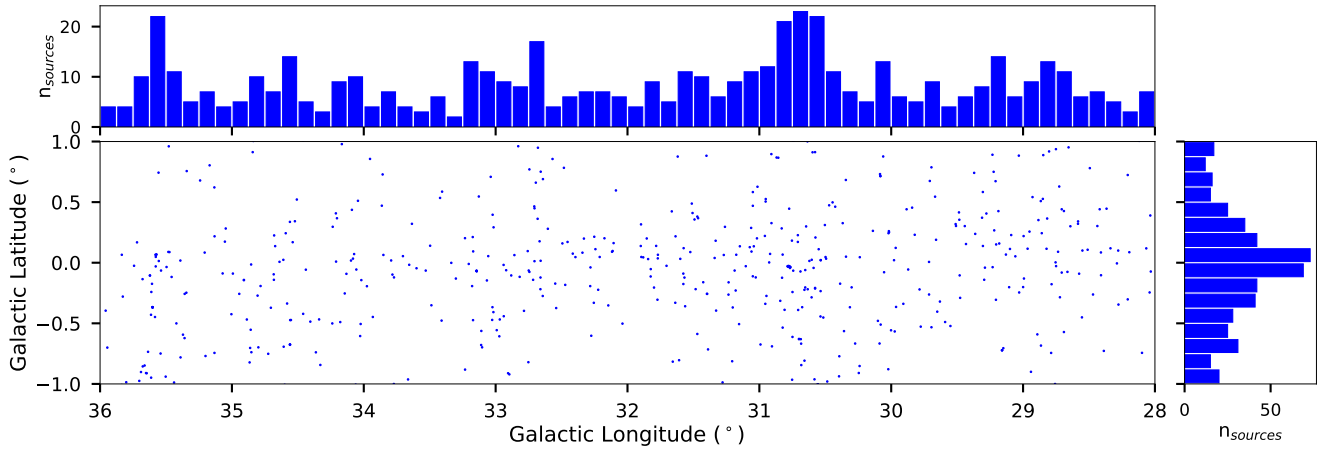

Fig. 4. Spatial distribution of radio sources detected in the B-configuration images that have no counterparts in the D-configuration images.

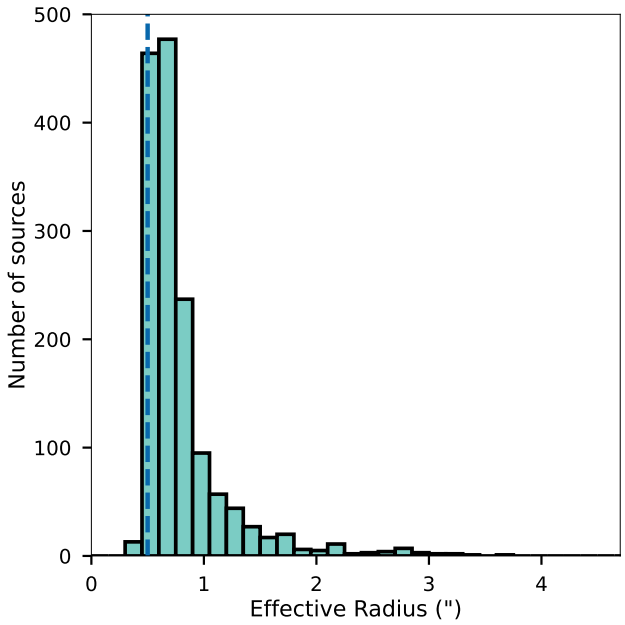

Fig. 5. Distribution of the source effective radius. The dash-dotted line indicates the resolution of the observations (half beam width). The images are only sensitive to angular scales ≤4.″1. The bin size used is 0.″15.

GLOSTAR D-configuration (Medina et al. 2019) and in the HI/OH/Recombination line survey of the Milky Way (THOR) survey (Bihr et al. 2016, described in the next section). To compare the different results, we selected the sources whose spectral indices were already determined and that have a point-like structure ($Y \leq 1.1$) in all three sets of results. The last constraint was imposed to diminish the effects of possible scale structure differences, as the GLOSTAR D-configuration and THOR have angular resolutions of 18″. Figure 8 shows the histogram distributions of the spectral index differences of the three sets. We found that the measured spectral indices are consistent among the three data sets, given that the mean of the differences is consistent with zero. We thus conclude that the spectral indices measured in the GLOSTAR B-configuration images are reliable.

In star forming regions (SFRs), three main mechanisms are known to produce compact radio continuum emission, and they are related to different astrophysical phenomena (Rodríguez et al. 2012). The majority of radio sources show thermal free-free radio continuum emission from ionized gas (e.g., HII regions, externally ionized globules, proplyds, jets) that has a spectral index ranging from 2.0 (optically thick) at low frequencies to −0.1 (optically thin) at high frequencies. Magnetically active low-mass stars may show nonthermal gyrosynchrotron with spectral indices ranging from −2.0 to +2.0. Nonthermal synchrotron emission arising from colliding winds in high-mass binaries, as well from jets ejected by high-mass stars interacting with the ambient interstellar medium (ISM), have a typical spectral index of −0.7. However, other phenomena not related to star formation also can produce thermal radio emission, namely gas ionized in planetary nebulae (PNe), while synchrotron emission is observed from extragalactic sources. Background active galactic nuclei (AGN) will mostly emit optically thin synchrotron emission with spectral indices ∼−0.7. On the other hand, a fraction (up to 20%) of extragalactic background radio sources show flat or positive spectral indices (e.g., Callingham et al. 2017). These represent a population of star forming galaxies and progenitors of AGN (i.e., high-frequency peakers Dallacasa et al. 2000; Dallacasa 2003). Given the diversity of the radio sources, to better understand their nature, information at other wavelengths is required. This will be discussed in the following subsection.

3.7. Counterparts at other wavelengths

To gain more insight into the nature of the radio sources, we searched for counterparts at shorter wavelengths. The search was focused on catalogs that could give us evidence for ionized gas, dense cold gas, and dust, which are indicators of massive young stars and the regions they form in. We now briefly describe the catalogs used in our search.

The APEX Telescope Large Area Survey of the Galaxy (ATLASGAL) observed the Galactic plane at a wavelength of 870 µm (345 GHz), and with an angular resolution of ∼20″ (Schuller et al. 2009). The emission at this wavelength is dominated by dense cool gas and dust. Several ATLASGAL source catalogs have been released by Contreras et al. (2013); Csengeri et al. (2014), and Urquhart et al. (2014), who list > 10,000 dense clumps. We compare here our results with the compact source catalog presented by Urquhart et al. (2014). The differences between the angular resolution of ATLASGAL and the observations presented here have to be taken into account. Thus, we used an offset of 18″ (roughly the beam size of ATLASGAL images) to consider an ATLASGAL source to be a potential

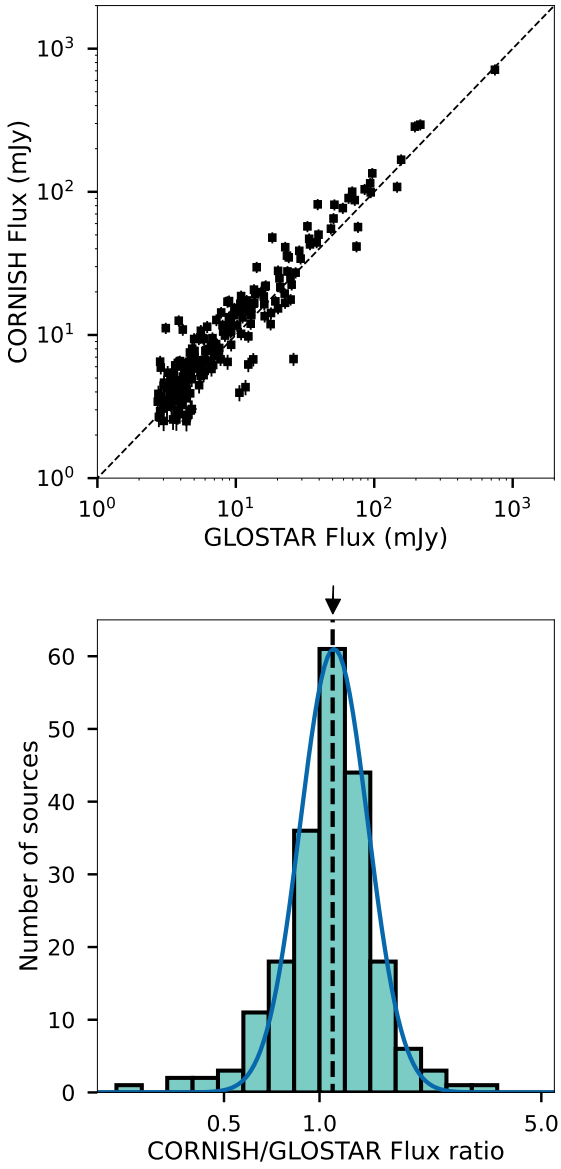

Fig. 6. Flux density comparison of GLOSTAR and CORNISH results. *Upper panel*: comparison of the peak flux densities of radio sources detected in GLOSTAR-B and CORNISH. *Lower panel*: histogram of the ratio between the peak flux densities of CORNISH and GLOSTAR. The width of the bars is 0.08 dex. The blue line indicates the model from the Gaussian fit to the histogram. The dashed line indicates the mean value of the distribution. The small arrow at the top of the plot shows the expected CORNISH/GLOSTAR flux density ratio for the different observed mean frequency.

counterpart for the compact radio source. We found 143 radio sources matching the position of 83 submillimeter sources.

The *Herschel* infrared Galactic plane survey (Hi-GAL) observed the inner Galaxy in five bands distributed in the wavelength range between 70 µm and 500 µm (Molinari et al. 2010, 2016). Notably, data taken at these wavelengths allow for determinations of the peak of the spectral energy distribution of cold dust, and thus the source temperatures. The Hi-GAL observations have angular resolutions from 10″ down to 35″ from the shortest to the longest wavelength. The median uncertainty of Hi-GAL sources is ∼1.″2. We used a 2″ offset between a Hi-GAL source and a GLOSTAR source to consider them as counterparts, and found 98 sources that matched this criterion.

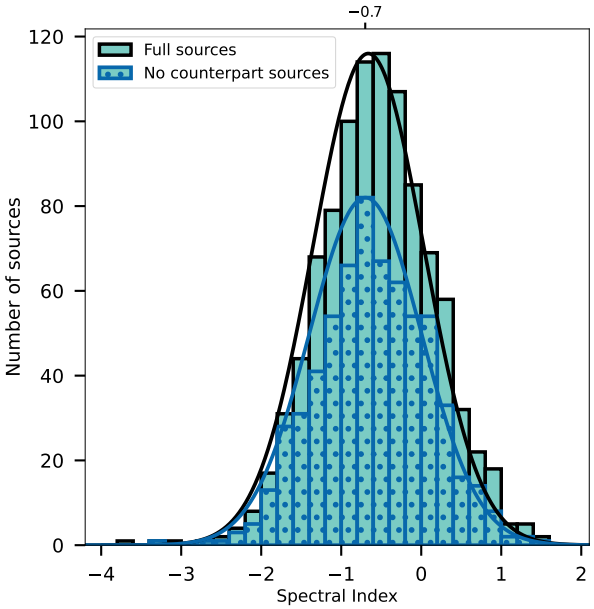

Fig. 7. Distribution of the in-band determined spectral indices. The blue dotted bars show the spectral index distribution of sources with no counterparts at any other wavelength.

The Wide-field Infrared Survey Explorer (WISE) mapped the entire sky in four infrared bands centered at 3.4, 4.6, 12.0, and 22.0 µm. The WISE ALL-sky Release Source Catalog contains astrometry and photometry for over half a billion objects (Wright et al. 2010). The angular resolution of the observations is 6″ at the shortest wavelength and the position errors are around 0.″2. To consider a WISE source as the counterpart to a GLOSTAR radio source, we used a maximum offset of 2″. A total of 125 sources match this criterion.

The Galactic Legacy Infrared Mid-Plane Survey Extraordinaire (GLIMPSE; Benjamin et al. 2003; Churchwell et al. 2009) mapped a large fraction of the Galactic plane with the *Spitzer* Space Telescope. It observed in four near-infrared sub-bands covering the range from 3.6 to 8.0 µm, and with angular resolutions of ∼2″. While the filter widths of the 3.6 and 4.5 µm bands are similar to those of WISE, the GLIMPSE survey focused on Galactic plane observations and is more sensitive than WISE. The ISM emission at these wavelengths comes mainly from warm and dusty embedded sources. Considering the angular resolution of our observations and the position uncertainties in the GLIMPSE survey, we used an offset of 2″ for the counterpart searching, leading to 251 matching sources.

The United Kingdom Infrared Deep Sky Survey (UKIDSS) is a suite of five public surveys at near-infrared wavelengths (NIR) of varying depth and area coverage (Lucas et al. 2008)[6]. In particular, the UKIDSS Galactic plane survey (UKIDS-GPS) covered a total of 1878 deg^2 of the northern hemisphere Galactic plane. The main observed bands are the so-called J- (1.25 µm), H- (1.65 µm), and K- (2.20 µm) bands. The spatial resolution of the UKIDSS-GPS observations is typically better than 0.″8. For the counterpart search of GLOSTAR radio sources in the UKIDSS-GPS catalog, we have used this value of 0.″8, finding 389 matches.

[6] The UKIDSS project is defined in Lawrence et al. (2007). UKIDSS uses the UKIRT Wide Field Camera (WFCAM; Casali et al. 2007). The photometric system is described in Hewett et al. (2006), and the calibration is described in Hodgkin et al. (2009). The pipeline processing and science archive are described in Hambly et al. (2008).

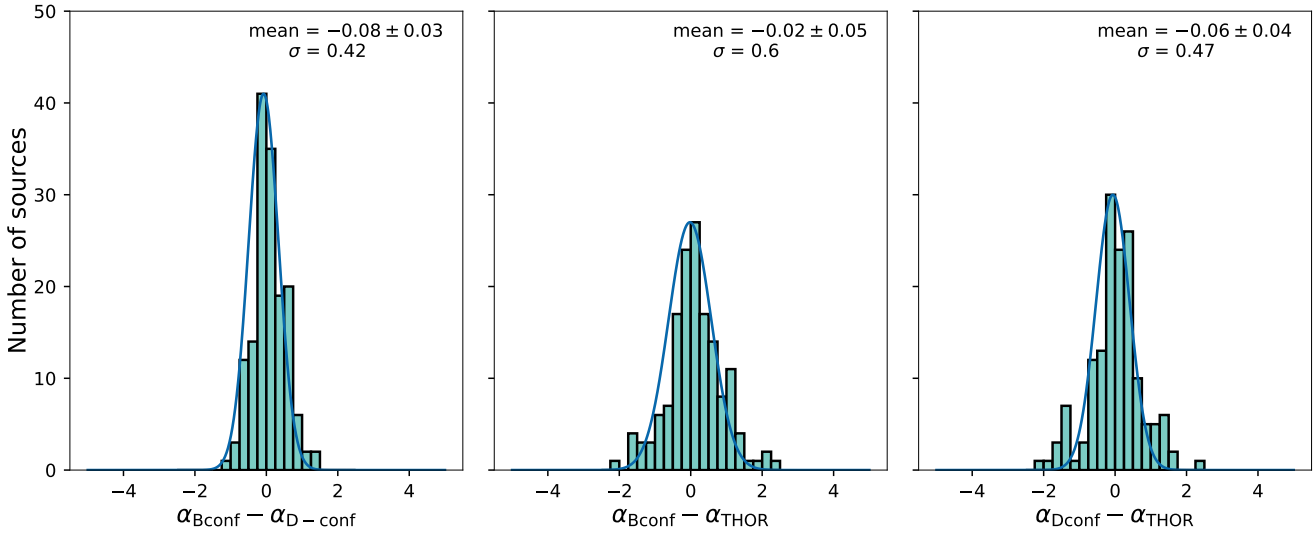

Fig. 8. Spectral index difference distributions. *From left to right*: GLOSTAR B-configuration and GLOSTAR D-configuration, GLOSTAR B-configuration and THOR, and GLOSTAR D-configuration and THOR.

After our careful search for counterparts at other wavelengths, it is noticeable that 640 radio sources have no counterparts at any other wavelength. The spectral index distribution of the sources in this category shows that they have preferably negative spectral indices (see Fig. 7). We further discuss these sources in the next section.

3.8. Classification of radio sources

Using the counterparts of the radio sources in the catalogs described in the previous section, a robust classification could be carried out. A single classification was performed for fragmented sources listed in Table 2 instead of separate classifications of their fragments, and thus the classification was performed for 1409 sources. The classification criteria were based on our findings of the emission properties and/or counterparts of near-infrared (NIR; UKIDSS), mid-infrared (MIR; GLIMPSE and WISE), far-infrared (FIR; Hi-Gal), and submillimeter (SMM; ATLASGAL) surveys.

Images from the abovementioned infrared surveys are plotted at the position of the radio sources; some examples can be seen in Appendix B. For the SMM and FIR surveys, we show the emission properties of each GLOSTAR source. For the NIR and MIR surveys, we did a visual inspection of the three-color images for the UKIDSS (red K-band, green H-band, and blue J-band), the GLIMPSE (red 8.0 µm, green 4.5 µm, and blue 3.6 µm), and the WISE (red 22.0 µm, green 12.0 µm and blue 4.6 µm) surveys. The sources have been classified into five groups, using the following criteria:

"HII region candidates": Radio sources with emission at SMM and FIR wavelengths, and with weak or no emission at MIR and NIR (Hoare et al. 2012; Anderson et al. 2012; Urquhart et al. 2013; Yang et al. 2021).

"Radio star": Compact radio sources showing blue compact emission in the three-color images of NIR and MIR wavelengths. Weak or no emission at FIR wavelenghts and no-emission at SMM wavelengths (Hoare et al. 2012; Lucas et al. 2008).

"Planetary nebula" (PN): Sources showing red emission in the three-color images of NIR and MIR wavelengths, where they are also seen as isolated point sources. Weak or no emission at FIR and SMM wavelengths (Hoare et al. 2012; Anderson et al. 2012; Phillips & Marquez-Lugo 2011).

"Photo dissociated region" (PDR): Ionized gas seen as extended emission at MIR, and showing only weak or no compact emission at FIR and SMM wavelengths (Hoare et al. 2012).

"Extragalactic candidate" (EgC): Radio sources that have no counterpart at any other wavelength, or are only seen as point sources at NIR wavelengths (Hoare et al. 2012; Lucas et al. 2008; Marleau et al. 2008).

"Other sources": Sources that could not be classified in any of the previous categories.

The number of radio sources in these groups are 93 HII region candidates, four PDRs, 83 radio stars, 65 PNe, 1163 EgCs, and two other sources. Examples of sources in these classes are shown in Figs. B.1–B.4. The individual source classification is given in Col. 17 in Table 1 and in Col. 5 of Table 2 for fragmented sources.

3.9. Sources previously classified

Classification of the radio sources is a main part of the catalog construction. However, some of the sources could have been previously classified. A search for previous classifications of the radio sources was performed using the SIMBAD astronomical database (Wenger et al. 2000), within a radius of 2″. We found that 269 radio sources have counterparts in the SIMBAD database. Most of these sources, 138, are only classified as radio sources, and are thus of an unknown nature. The classification of the remaining 107 sources suggests that these are Galactic sources. In Table 3 we have separated these sources into seven types of sources, and have listed the source class in SIMBAD considered for these types and the number of sources of each type.

4. Discussion

4.1. Overview of the final classification

The final radio source classification is a combination of the method described in Sect. 3.8 and the use of known information of individual sources recovered from the SIMBAD database. For our final catalog, we additionally considered the SIMBAD

Table 3. Source classification from the SIMBAD database.

Type	SIMBAD class [(a)]	#
Evolved stars	WR*, PN, PN?, AB?, CV*	38
Pulsars	Psr	3
Stars	*, Cl*	7
Young stellar objects	Y*O, Y*?	30
HII regions	HII	28
Gamma-ray source	gam	1
Extragalactic objects	QSO	1
Other objects	Mas, mm, smm, IR, NIR, MIR, MoC, EmO, PoC, cor	23

Notes. [(a)]The SIMBAD object classification is described in http://simbad.u-strasbg.fr/simbad/sim-display?data=otypes.

Table 4. Final source classification of radio sources.

Classification	#
HII region candidates	93
WR	2
Pulsar	3
Radio stars	81
PNe	64
Cataclysmic variable	1
PDRs	4
Other	2
EgCs	1157

classification for sources for which we found no counterpart in the IR and submillimeter catalogs that we searched. This was, for example, the case for pulsars that are usually not detected at infrared wavelengths and are nonthermal radio emitters. Based on the criteria described in the previous section, they were first classified as EgCs and after consulting the SIMBAD database, they were finally classified as pulsars. A similar situation occurred with a Wolf–Rayet star and a cataclysmic variable star, wherein they were initially classified as a PN and as a Radio star, respectively. We used the classification recovered from SIMBAD in these cases.

In Table 4 we give the number of sources found in each of the classifications. Interesting sources are the HII region candidates, as they are related to MSF, which we discuss later.

4.2. Comparison of classifications

Classifications of some of the detected radio sources were performed in previous radio surveys and here we compare the results of these classifications. We focus on a comparison based on the low-resolution GLOSTAR D-configuration image presented by Medina et al. (2019), and with the classification based on the CORNISH survey, which has a similar angular resolution observation to our B-configuration data (Purcell et al. 2013).

4.2.1. GLOSTAR D-configuration

Some differences between the present catalog and the one derived from the D-configuration data are expected, since for the latter, the search for counterparts was carried out using larger angular separations than in this work, on account of the lower resolution. Fifty-four of the HII region candidates identified by us were also detected in D-configuration images, and were also identified as HII regions. Four other HII region candidates had a D-configuration counterpart, but were unclassified. The remaining 32 HII region candidates were not detected in the D-configuration images. Additionally, six sources classified as HII region candidates in the D-configuration catalog have been classified as PNe in the present work, as their positions are no longer coincident with ATLASGAL sources.

We detected 32 radio sources that were classified as PNe in the D-configuration catalog, of which 30 are classified as PNe in this work; one is classified as a WR star and another as an EgC because it is no longer positionally coincident with IR emission. We also detected 13 sources identified as radio stars in the D-configuration, of which ten were related to a radio source also classified as a radio star. The remaining source, G028.098–00.781, was resolved into three different sources; two of them were classified as extragalactic sources and the other as a PN. A further 749 sources detected in D-configuration images were also detected in the B-configuration images. Among these, 688 were classified as EgCs, consistent with the suggestion by Medina et al. (2019) that most of their unclassified radio sources are background extragalactic radio sources. The remaining 61 unclassified sources in D-configuration have now been classified: 43 as radio stars, 14 as PNe, and four as HII region candidates. A comparison between the method used in the D-configuration data and in the B-configuration data shows a consistency of better than 90% in the resulting classes.

4.2.2. CORNISH survey

The CORNISH survey has a similar angular resolution to the GLOSTAR B-configuration and it also used IR information to classify detected radio sources. In their classification effort, they considered UCHII regions and dark HII regions; we detected radio emission from 40 CORNISH sources classified as UCHII and from one dark HII region, which are classified as HII region candidates by us. We also detected 25 CORNISH radio sources classified as PNe that are also classified as PNe in our work. Seventeen radio stars in the CORNISH survey have counterparts in our catalog; we classified fifteen of them also as radio stars and two of them as EgCs because we did not find IR counterparts. We detected 171 CORNISH radio sources classified as IR-Quiet (not detected at IR wavelengths); we classify 167 of them as EgCs, four as radio stars, as IR emission is now reported in the position of these sources, and one as a pulsar, based on the SIMBAD database. Finally, out of the 29 radio-Galaxy sources in CORNISH, 28 are classified as EgCs in our work, and the remaining source is classified as radio star, given its IR properties. The consistency in classification between the CORNISH survey and the GLOSTAR B-configuration is high, especially for HII regions and PNe where we found a 100% agreement.

4.2.3. THOR survey

The THOR survey (Bihr et al. 2015; Beuther et al. 2016; Wang et al. 2020) observed the northern hemisphere of the Galactic plane with the VLA in C-configuration and using its *L*-band receivers (1 to 2 GHz). It covered Galactic longitudes from 14.°5 to 67.°4 and Galactic latitudes from −1.°25 to 1.°25, that is to say, including the area of the maps presented in this paper. The angular resolution of the THOR radio continuum images is 25″ and they have noise levels from 0.3 to 1.0 mJy beam^{-1} (Wang et al. 2018). While a detailed comparison of the source classification

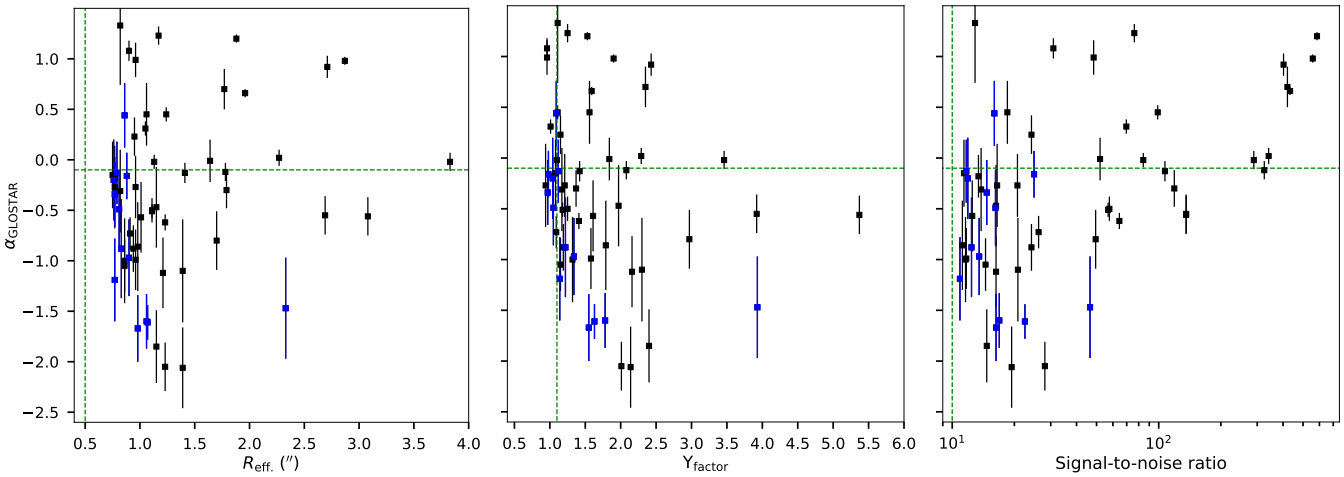

Fig. 9. Spectral index of identified HII region candidates as a function of the effective radius (*left*), *Y*-factor (*center*), and S/N (*right*). Black symbols are sources that are related to previously identified HII regions and blue symbols are the new identified HII region candidates.

by the THOR survey and GLOSTAR B-configuration is limited, given the different image angular scales, it is still useful.

To compare GLOSTAR B-configuration sources with THOR sources, we used a maximum separation of 2.″5, which is the position accuracy of the THOR survey (Wang et al. 2018). We found 554 sources matching in position between these surveys. From these sources, the THOR survey identified 34 HII regions (26 of which are identified as HII region candidates) and nine as PNe (also identified as PNe with our classification criteria). Our classification for the remaining eight sources identified as HII regions by the THOR survey is four EgCs and four PNe. Differences between the classification of these sources can be caused by the different angular scales used for comparison with IR surveys. In fact, the median match radius of IR HII regions (identified with the WISE survey; Anderson et al. 2014) with the THOR survey is ∼60″ (Wang et al. 2018), almost two orders of magnitude larger than our angular resolution.

4.3. HII region candidates

We identified 93 HII region candidates[7]. Out of these sources, 71 were previously related to HII regions from our analysis of the D-configuration images, or from the CORNISH or THOR surveys, or from the SIMBAD database, and 22 are new detections from this work. A characteristic of the radio emission from HII regions is that the spectral index values ranges from −0.1 (optically thin free-free radio emission) to 2.0 (optically thick free-free radio emission). Observationally, the spectral index distribution of hundreds of young HII regions at similar frequencies show a mean value of 0.6 (Yang et al. 2019, 2021). We determined the in-band spectral index (see Sect. 3.6) for 57 HII region candidates, 13 of which are new. In Fig. 9, we plot the spectral index of these HII regions as a function of the $R_{\rm eff}$, the *Y*-factor, and the S/N. Surprisingly, some of the determined spectral indices are negative and well below the lowest value expected for the free-free radio emission of $\alpha = -0.1$, indicating that the radio emission nature is nonthermal. The results are not affected by the size of the source, as most of them are slightly resolved sources ($R_{\rm eff} \simeq \theta_{\rm resolution}/2 = 0.''50$).

[7] To show the MIR emission around the position of these sources, a series of images are presented in Appendix C.

Kalcheva et al. (2018) obtained the spectral index for known ultracompact HII regions and found that about 18% of their sample were consistent with negative spectral indices. They discuss their results and conclude that different interferometer array configurations and time variability could explain these negative values. These effects, however, are not present in the GLOSTAR observations presented here. Hence, these radio sources with negative spectral indices could be related to HII regions but they are not the HII regions themselves (e.g., Purser et al. 2016).

Compact radio sources have been found to be related to HII regions. The best-known and closest case is the Orion Nebula Cluster (ONC), where around 600 compact radio sources are found in the HII region ionized by the Trapezium stars (Forbrich et al. 2016; Vargas-González et al. 2021). As first suggested by Garay et al. (1987); Garay (1987), most of these fall into two broad categories: first, sources with thermal radio emission from circumstellar matter, often protoplanetary disks ("Proplyds"), which are photo-evaporated in the intense UV field of the brightest Trapezium star θ^1 Ori C (O7Vp); second, nonthermal sources associated with the coronal activity of magnetically active low-mass members of the ONC, many of which also show X-ray emission and are (highly) variable (Forbrich et al. 2021; Dzib et al. 2021). Other example regions are NGC 6334 (Medina et al. 2018) and the M17 (Rodríguez et al. 2012) SFRs, where several radio sources are found close to prominent HII regions. Also, in these SFRs a significant fraction of the compact radio sources have been found to produce nonthermal emission. That a high number of such radio sources can be detected on the ONC is a result of the cluster's close distance, *D*, of just ≈400 pc (Menten et al. 2007; Kounkel et al. 2017). Extrapolating the Orion case to a distance of a few kiloparsecs, most of these magnetically active stars would not be detected, except for the two strongest sources with measured integrated flux densities of a few tens of mJy. We note that NGC 6334 and M17, mentioned above, are also relatively nearby, at $D = 1.34^{+0.15}_{-0.12}$ and $1.98^{+0.14}_{-0.12}$ kpc, respectively (Reid et al. 2014; Wu et al. 2014). Time variable weak radio sources around the well-studied ultracompact HII region W3(OH) ($D = 2.0$ kpc) are other examples (Wilner et al. 1999). For more distant SFRs, thermal radio emission is only detected from the HII region itself, which is excited by the central high-mass star(s) of a cluster.

It should be noted that other phenomena can produce compact nonthermal radio emission in massive SFRs that are at work

in Orion and can be observed in regions at distances of a few kpc, such as nonthermal radio jets (e.g., Carrasco-González et al. 2010; Purser et al. 2016) and wind collision regions in massive binary stars (e.g., Dzib et al. 2013). Nonthermal radio jets from young stellar objects, however, are rare and only a handful of cases are known. Similarly, nonthermal radio emission from wind collision regions are not common and are usually associated with evolved massive stars that have powerful winds.

On the other hand, the radio sources with positive spectral indices could be true HII regions. More extensive multiwavelength radio analysis is needed to characterize their emission and determine, for example, their turnover frequency and their emission measure. In general, all the radio sources that are associated with HII regions discussed in this work deserve further attention and more detailed studies.

4.4. Variable radio sources

By comparing the peak flux densities measured in the GLOSTAR images with those reported in CORNISH (Purcell et al. 2013), we looked for sources with variable radio emission. The search was restricted to sources with $Y < 2.0$ (i.e., with compact radio emission). Variability was identified when the source was detected in both catalogs, GLOSTAR and CORNISH, but the flux ratio was larger than 2.0. We also identified variability when we detected a source in the GLOSTAR catalog with a peak flux density level >2.7 mJy beam^{-1} (the CORNISH detection limit) and it is not reported in the CORNISH catalog. Finally, a source detected as unresolved in the CORNISH catalog that is not in the GLOSTAR high-reliability catalog or in the catalog of sources with 5 to 7σ, was also considered as a variable radio source.

With the above criteria, we identified 49 variable sources. They are listed in Table 5, together with the peak flux densities in the compared catalogs. The GLOSTAR and CORNISH classifications are listed when available. Most of the identified variable radio sources are EgC or IR-quiet sources, and were only detected at radio wavelengths. Since extragalactic background sources are not expected, in general, to show pronounced variability, some of these sources could be interesting Galactic radio sources whose nature should be explored.

4.5. Extragalactic objects

As has been shown in our previous works, most of the detected radio sources are expected to be background extragalactic objects (Medina et al. 2019; Chakraborty et al. 2020). Following the formulation by Fomalont et al. (1991) and using an observed area of 57,600 arcmin^2, assuming a nominal noise level of σ = 65 μJy beam^{-1} and a threshold 7× the noise level, we estimate that the number of expected background extragalactic sources in our image is 1138 ± 664. This number suggests that most of the detected radio sources above 455 μJy beam^{-1} (7σ) are of extragalactic origin.

From our classification criteria, we compiled a list of 1159 sources that most probably have an extragalactic origin. They are labeled as EgC in Table 1. Their extragalactic nature is also supported by the negative spectral index of most of them. The spectral index was determined for 777 of these sources and 157 (20%) have a flat or positive spectral index, consistent with the expected number of extragalactic radio objects that are expected to have positive spectral indices at our frequencies.

Similar to our previous work (Chakraborty et al. 2020), we also studied the Euclidean-normalized differential source counts of the point sources characterized as being extragalactic in origin. We binned the source integrated flux densities in logarithmic space and divided the raw counts in each bin by the fraction of image area over which a source with a given integrated flux density value can be detected, known as the visibility area (Windhorst et al. 1985). The differential source counts were calculated by dividing the visibility area weighted source counts in each bin by the total image area (Ω in steradians) and bin width (ΔS in Jy). These differential source counts were normalized by multiplying with $S^{2.5}$, where S is the mean integrated flux density of sources in each bin (Windhorst et al. 1985). The normalized differential source counts is shown in Fig. 10, where the error bars are Poissonian. We compared our findings with two simulated catalogs, the SKA Design Study simulations (SKADS, Wilman et al. 2008) and the Tiered Radio Extragalactic Continuum Simulations (T-RECS, Bonaldi et al. 2019). We also compared our findings with the observed extragalactic source populations at low frequency as well as at high frequency, which include: the TIFR GMRT Sky Survey at 150 MHz (TGSS-ADR1; Intema et al. 2017), the BOOTES field at 150 MHz using LOFAR (Williams et al. 2016), the Lockman Hole field at 1.4 GHz with the LOFAR (Prandoni et al. 2018), the COSMOS field at 3 GHz with the VLA (Smolčić et al. 2017), the ECDFS field at 5 GHz (Huynh et al. 2015) and 9 GHz (Huynh et al. 2020) with ATCA, and the 1.4 GHz source counts based on observations with the VLA by Condon (1984). In all cases we scaled the source counts to 5.8 GHz using a spectral index, $\alpha = -0.7$. We found that the source count of these sources classified as extragalactic in the GLOSTAR survey is statistically similar and consistent with the previously observed extragalactic source population, as well as with the simulated catalogs. This shows that the majority of these sources are indeed of extragalactic origin.

4.6. Perspective on the search of nonthermal Galactic sources

Figure 7 shows that the peak of the spectral index distribution is -0.66 ± 0.02. As discussed in the previous subsection, most of the unidentified radio sources will be of extragalactic origin, but some of these will be interesting Galactic nonthermal radio sources. These sources are only detected at radio frequencies and it will be hard to distinguish them.

Very Long Baseline Interferometry (VLBI) observations to all unidentified compact radio sources could help to distinguish the Galactic from the extragalactic radio sources. Position measurements on the scale of several months to years could measure the proper motions and trigonometric parallaxes of these sources. As the extragalactic background sources are not expected to exhibit proper motions or trigonometric parallaxes, these observations can help to distinguish between the two classes of radio sources. A wide field VLBI survey of the Galactic plane is now feasible thanks to the DiFX software correlator (Deller et al. 2011), which enables multiple-phase center correlation inside the primary beam of the interferometer.

Radio continuum observations can be used to search for pulsar candidates (e.g., Maan et al. 2018). The advantage of these observations compared to conventional pulsar searches is that they require less computational power. The observed frequency by the GLOSTAR survey also has the advantage that the radio emission is less affected by scattering than the lower frequencies used for conventional pulsar searches. As an interesting example, the radio emission from PSR J1813–1749, one of the most energetic known pulsars, was first detected in radio continuum

Table 5. Variable radio sources.

Source name	GLOSTAR			CORNISH		
	$S_{\rm peak}$ (mJy beam^{-1})	$\sigma_{S_{\rm peak}}$	Classification	$S_{\rm peak}$ (mJy beam^{-1})	$\sigma_{S_{\rm peak}}$	Classification
(1)	(2)	(3)	(4)	(5)	(6)	(7)
G028.1875+00.5047	...			2.61	0.39	IR-Quiet
G028.3660–00.9640				2.92	0.48	IR-Quiet
G028.4012+00.4776				5.25	0.60	Radio-Galaxy
G028.6043–00.6530	2.79	0.17	EgC			
G028.9064+00.2548				3.47	0.53	IR-Quiet
G028.9224–00.6589	5.07	0.29	EgC			
G029.1640–00.7922	3.05	0.18	EgC			
G029.2620+00.2916				2.76	0.45	IR-Quiet
G029.3096+00.5124				2.84	0.43	IR-Quiet
G029.4302–00.9967				2.83	0.48	IR-Quiet
G029.4404–00.3199				2.81	0.47	IR-Quiet
G029.4959–00.3000	5.43	0.30	EgC			
G029.5184+00.9478				2.43	0.40	IR-Quiet
G029.5780–00.2686	12.31	0.69	PN	6.22	0.72	PN
G029.5893+00.5789	1.73	0.12	EgC	4.17	0.50	IR-Quiet
G030.2193+00.6501				2.80	0.42	IR-Quiet
G030.3704+00.4824	2.83	0.16	HII			
G030.6328–00.7232				2.57	0.40	IR-Quiet
G030.6517–00.0605	3.08	0.21	PN			
G030.7859–00.0298	3.72	0.35	Other			
G030.9704–00.7436				2.47	0.38	IR-Quiet
G031.0025–00.6330	2.78	0.17	EgC			
G031.0450–00.0949				2.63	0.40	IR-Quiet
G031.0777+00.1703	13.37	0.74	EgC	6.75	0.72	IR-Quiet
G031.2989–00.4929	3.43	0.21	Radio-star			
G031.3444–00.4625				2.78	0.37	IR-Quiet
G031.3917+01.0265				2.39	0.38	Radio-Star
G031.3993–00.0813	5.31	0.30	EgC			
G031.5694+00.6870	26.11	1.44	EgC	6.79	0.71	IR-Quiet
G031.9943+00.5156	3.14	0.18	EgC			
G032.2739–00.0358	2.91	0.17	EgC			
G032.3843–00.3397	3.95	0.23	EgC			
G032.4536+00.3679	1.42	0.10	EgC	2.74	0.46	IR-Quiet
G032.5898–00.4469	3.14	0.18	EgC			
G032.5996+00.8265	2.87	0.17	EgC	5.92	0.62	IR-Quiet
G032.7396+00.8344	2.78	0.16	EgC			
G032.7568+00.0959	2.76	0.18	EgC			
G033.1860+00.9528	2.86	0.17	EgC			
G033.3513+00.4056				2.62	0.40	IR-Quiet
G033.4100–00.4775	3.05	0.18	EgC			
G033.4584+00.0163	3.82	0.22	EgC			
G033.8964+00.3251	2.87	0.17	Radio-star			
G033.9622–00.4966				2.81	0.42	IR-Quiet
G034.2171–00.6886				2.16	0.34	IR-Quiet
G034.4794–00.1683	2.78	0.16	EgC			
G034.7242+00.6660	2.8	0.17	EgC			
G035.0605+00.6208				2.76	0.43	IR-Quiet
G035.2618+00.1079				2.36	0.39	IR-Quiet
G035.9038–00.4810	2.26	0.14	EgC	4.94	0.55	IR-Quiet

Notes. Names for sources not detected in GLOSTAR images come from the CORNISH catalog (Purcell et al. 2013).

images at 5 GHz (Dzib et al. 2010, 2018), while searches for the pulsed radio emission at lower frequencies failed (Helfand et al. 2007; Halpern et al. 2012; Dzib et al. 2018). It turns out that interstellar scattering in the direction of this pulsar is very high, and PSR J1813–1749 is the most heavily scattered known pulsar (Camilo et al. 2021). Pulsar radio continuum emission is characterized by a point-like structure and a steep radio spectrum ($\alpha = -1.4 \pm 1.0$; Bates et al. 2013). These are criteria that are shared with EgCs in our classification scheme, making them hard to differentiate. Dedicated observations to search for pulsed emission can distinguish them, with the advantage that the observations will be target intended instead of a blind survey.

5. Conclusions

As part of the GLOSTAR survey, the VLA in its B- and D-configurations was used to observe a large portion of the Galactic plane in the *C*-band. In this paper we present the B-array observations covering the area within $28^\circ \leq \ell < 36^\circ$ and $|b| < 1^\circ$, which we previously investigated using data obtained in

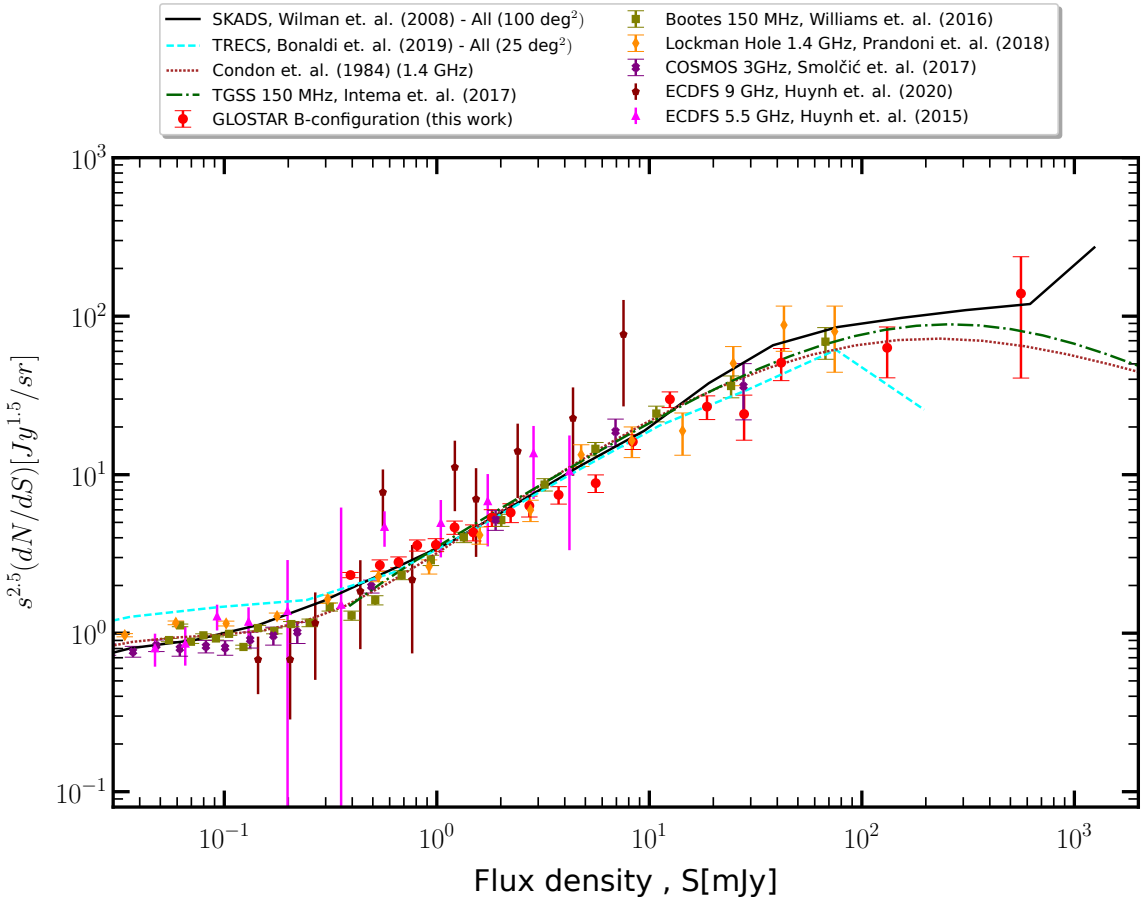

Fig. 10. Euclidean-normalized differential source counts of the point sources classified as of extragalatic origin in the GLOSTAR survey. We compare the source counts with the simulated radio sky and previously observed source populations. For details of simulated catalogs and different observed source populations, see the text.

the D-configuration (Medina et al. 2019). Using a combination of automatic source extraction with BLOBCAT (Hales et al. 2012) and visual inspection, we identified 3325 radio sources.

The catalog of these radio sources is divided into two parts. The catalog of highly reliable radio sources contains 1457 entries. Detailed properties of these sources are given, such as their positions, S/N, integrated and peak fluxes, the ratio between these two values (also known as the Y-factor), the effective radii, and the spectral indices. The weak source catalog lists 1866 sources with a S/N between 5 to 7. Only their basic properties such as their positions, S/N, and integrated and peak fluxes are given.

The highly reliable radio sources were further investigated. The positions of these sources were compared with the positions from the CORNISH catalog (Purcell et al. 2013) and radio sources detected with the VLBI from the Radio Fundamental catalog. We found that the positions of GLOSTAR sources are in agreement with those in these catalogs to better than 0.″1. We also compared our integrated flux densities with those in the CORNISH catalog and conclude that the GLOSTAR integrated flux densities are accurate to within 10%, apart from clearly variable sources. From a comparison with the GLOSTAR D-configuration catalog, we find that 908 of them are related to 780 sources detected in the D-configuration images. In particular, 22 D-configuration sources are partially resolved and appear as fragmented sources in the new high-resolution images. A total of 72 highly reliable B-configuration sources comprise these 22 fragmented sources.

To further investigate the nature of the highly reliable radio sources, we used information from surveys at infrared and submillimeter wavelengths, as well as consulting the SIMBAD database. The classification of the radio sources resulted in 93 HII region candidates, 64 PNe, 81 radio stars, and most of the remaining sources as EgCs. We compared our classification with the classification for the D-configuration radio sources, and for the sources from the CORNISH survey. We find that the classification from the catalogs agree for more than 90% of the sources. An interesting result is that many sources classified as HII region candidates, however, have a negative in-band spectral index, suggesting that the radio emission is predominantly non-thermal, and thus they are not the HII regions themselves, but likely related to nearby YSOs. These sources could be other radio emitter objects related to star formation. They deserve further study, using deeper and radio multiwavelength observations to better characterize their radio emission nature, and the nature of the objects themselves. Finally, by comparing the integrated flux densities from GLOSTAR and CORNISH, whose observations are separated by 7 yr, we identified 49 variable sources, whose nature should be explored for most of these sources.

Acknowledgments. We would like to thank the Anonymous Referee for his/her valuable comments and suggestions on our manuscript. This research was partially funded by the ERC Advanced Investigator Grant GLOSTAR (247078). AY would like to thank the help of Philip Lucas and Read Mike when using the data of the UKIDSS survey. RD and HN are members of the International Max Planck Research School (IMPRS) for Astronomy and Astrophysics at the Universities of Bonn and Cologne. HB acknowledges support from the

European Research Council under the Horizon 2020 Framework Program via the ERC Consolidator Grant CSF-648505. HB also acknowledges support from the DFG in the Collaborative Research Center SFB 881 – Project-ID 138713538 – "The Milky Way System" (subproject B1). VY acknowledges the financial support of CONACyT, México. This work (partially) uses information from the GLOSTAR database at http://glostar.mpifr-bonn.mpg.de supported by the MPIfR, Bonn. It also made use of information from the ATLASGAL database at http://atlasgal.mpifr-bonn.mpg.de/cgi-bin/ATLASGAL_DATABASE.cgi supported by the MPIfR, Bonn, as well as information from the CORNISH database at http://cornish.leeds.ac.uk/public/index.php which was constructed with support from the Science and Technology Facilities Council of the UK. This work is based in part on observations made with the *Spitzer* Space Telescope, which is operated by the Jet Propulsion Laboratory, California Institute of Technology under a contract with NASA. This publication also makes use of data products from the Wide-field Infrared Survey Explorer, which is a joint project of the University of California, Los Angeles, and the Jet Propulsion Laboratory/California Institute of Technology, funded by the National Aeronautics and Space Administration. *Herschel* is an ESA space observatory with science instruments provided by European-led Principal Investigator consortia and with important participation from NASA. This research has made use of the SIMBAD database, operated at CDS, Strasbourg, France. We have used the collaborative tool Overleaf available at: https://www.overleaf.com/

References

Anderson, L. D., Zavagno, A., Barlow, M. J., García-Lario, P., & Noriega-Crespo, A. 2012, A&A, 537, A1
Anderson, L. D., Bania, T. M., Balser, D. S., et al. 2014, ApJS, 212, 1
Bates, S. D., Lorimer, D. R., & Verbiest, J. P. W. 2013, MNRAS, 431, 1352
Benjamin, R. A., Churchwell, E., Babler, B. L., et al. 2003, PASP, 115, 953
Bertin, E., & Arnouts, S. 1996, A&AS, 117, 393
Beuther, H., Bihr, S., Rugel, M., et al. 2016, A&A, 595, A32
Bihr, S., Beuther, H., Ott, J., et al. 2015, A&A, 580, A112
Bihr, S., Johnston, K. G., Beuther, H., et al. 2016, A&A, 588, A97
Bonaldi, A., Bonato, M., Galluzzi, V., et al. 2019, MNRAS, 482, 2
Brunthaler, A., Menten, K. M., Dzib, S. A., et al. 2021, A&A, 651, A85
Callingham, J. R., Ekers, R. D., Gaensler, B. M., et al. 2017, ApJ, 836, 174
Camilo, F., Ransom, S. M., Halpern, J. P., & Roshi, D. A. 2021, ApJ, 917, 67
Carey, S. J., Noriega-Crespo, A., Mizuno, D. R., et al. 2009, PASP, 121, 76
Carrasco-González, C., Rodríguez, L. F., Anglada, G., et al. 2010, Science, 330, 1209
Casali, M., Adamson, A., Alves de Oliveira, C., et al. 2007, A&A, 467, 777
Chakraborty, A., Roy, N., Wang, Y., et al. 2020, MNRAS, 492, 2236
Churchwell, E., Babler, B. L., Meade, M. R., et al. 2009, PASP, 121, 213
Condon, J. J. 1984, ApJ, 287, 461
Contreras, Y., Schuller, F., Urquhart, J. S., et al. 2013, A&A, 549, A45
Cotton, W. D. 2008, PASP, 120, 439
Csengeri, T., Urquhart, J. S., Schuller, F., et al. 2014, A&A, 565, A75
Dallacasa, D. 2003, PASA, 20, 79
Dallacasa, D., Stanghellini, C., Centonza, M., & Fanti, R. 2000, A&A, 363, 887
Deller, A. T., Brisken, W. F., Phillips, C. J., et al. 2011, PASP, 123, 275
Dokara, R., Brunthaler, A., Menten, K. M., et al. 2021, A&A, 651, A86
Dzib, S., Loinard, L., & Rodríguez, L. F. 2010, Rev. Mex. Astron. Astrofis., 46, 153
Dzib, S. A., Rodríguez, L. F., Loinard, L., et al. 2013, ApJ, 763, 139
Dzib, S. A., Rodríguez, L. F., Karuppusamy, R., Loinard, L., & Medina, S.-N. X. 2018, ApJ, 866, 100
Dzib, S. A., Forbrich, J., Reid, M. J., & Menten, K. M. 2021, ApJ, 906, 24
Fomalont, E. B., Windhorst, R. A., Kristian, J. A., & Kellerman, K. I. 1991, AJ, 102, 1258
Forbrich, J., Rivilla, V. M., Menten, K. M., et al. 2016, ApJ, 822, 93
Forbrich, J., Dzib, S. A., Reid, M. J., & Menten, K. M. 2021, ApJ, 906, 23
Garay, G. 1987, Rev. Mex. Astron. Astrofis., 14, 489
Garay, G., Moran, J. M., & Reid, M. J. 1987, ApJ, 314, 535
Greisen, E. W. 2003, Astrophys. Space Sci. Lib., 285, 109
Hales, C. A., Murphy, T., Curran, J. R., et al. 2012, MNRAS, 425, 979
Halpern, J. P., Gotthelf, E. V., & Camilo, F. 2012, ApJ, 753, L14
Hambly, N. C., Collins, R. S., Cross, N. J. G., et al. 2008, MNRAS, 384, 637
Helfand, D. J., Gotthelf, E. V., Halpern, J. P., et al. 2007, ApJ, 665, 1297
Hewett, P. C., Warren, S. J., Leggett, S. K., & Hodgkin, S. T. 2006, MNRAS, 367, 454
Hoare, M. G., Purcell, C. R., Churchwell, E. B., et al. 2012, PASP, 124, 939
Hodgkin, S. T., Irwin, M. J., Hewett, P. C., & Warren, S. J. 2009, MNRAS, 394, 675
Huynh, M. T., Bell, M. E., Hopkins, A. M., Norris, R. P., & Seymour, N. 2015, MNRAS, 454, 952
Huynh, M. T., Seymour, N., Norris, R. P., & Galvin, T. 2020, MNRAS, 491, 3395
Intema, H. T., Jagannathan, P., Mooley, K. P., & Frail, D. A. 2017, A&A, 598, A78
Kalcheva, I. E., Hoare, M. G., Urquhart, J. S., et al. 2018, A&A, 615, A103
Kounkel, M., Hartmann, L., Loinard, L., et al. 2017, ApJ, 834, 142
Lawrence, A., Warren, S. J., Almaini, O., et al. 2007, MNRAS, 379, 1599
Lucas, P. W., Hoare, M. G., Longmore, A., et al. 2008, MNRAS, 391, 136
Maan, Y., Bassa, C., van Leeuwen, J., Krishnakumar, M. A., & Joshi, B. C. 2018, ApJ, 864, 16
Marleau, F. R., Noriega-Crespo, A., Paladini, R., et al. 2008, AJ, 136, 662
Medina, S. N. X., Dzib, S. A., Tapia, M., Rodríguez, L. F., & Loinard, L. 2018, A&A, 610, A27
Medina, S. N. X., Urquhart, J. S., Dzib, S. A., et al. 2019, A&A, 627, A175
Menten, K. M., Reid, M. J., Forbrich, J., & Brunthaler, A. 2007, A&A, 474, 515
Molinari, S., Swinyard, B., Bally, J., et al. 2010, PASP, 122, 314
Molinari, S., Schisano, E., Elia, D., et al. 2016, A&A, 591, A149
Nguyen, H., Rugel, M. R., Menten, K. M., et al. 2021, A&A, 651, A88
Nguyen, H., Rugel, M. R., Murugeshan, C., et al. 2022, A&A, 666, A59
Ortiz-León, G. N., Menten, K. M., Brunthaler, A., et al. 2021, A&A, 651, A87
Phillips, J. P., & Marquez-Lugo, R. A. 2011, MNRAS, 410, 2257
Prandoni, I., Guglielmino, G., Morganti, R., et al. 2018, MNRAS, 481, 4548
Purcell, C. R., Hoare, M. G., Cotton, W. D., et al. 2013, ApJS, 205, 1
Purser, S. J. D., Lumsden, S. L., Hoare, M. G., et al. 2016, MNRAS, 460, 1039
Reid, M. J., Menten, K. M., Brunthaler, A., et al. 2014, ApJ, 783, 130
Rodríguez, L. F., González, R. F., Montes, G., et al. 2012, ApJ, 755, 152
Schuller, F., Menten, K. M., Contreras, Y., et al. 2009, A&A, 504, 415
Smolčić, V., Delvecchio, I., Zamorani, G., et al. 2017, A&A, 602, A2
Urquhart, J. S., Thompson, M. A., Moore, T. J. T., et al. 2013, MNRAS, 435, 400
Urquhart, J. S., Csengeri, T., Wyrowski, F., et al. 2014, A&A, 568, A41
Vargas-González, J., Forbrich, J., Dzib, S. A., & Bally, J. 2021, MNRAS, 506, 3169
Wang, Y., Bihr, S., Rugel, M., et al. 2018, A&A, 619, A124
Wang, Y., Beuther, H., Rugel, M. R., et al. 2020, A&A, 634, A83
Wenger, M., Ochsenbein, F., Egret, D., et al. 2000, A&AS, 143, 9
Williams, W. L., van Weeren, R. J., Röttgering, H. J. A., et al. 2016, MNRAS, 460, 2385
Wilman, R. J., Miller, L., Jarvis, M. J., et al. 2008, MNRAS, 388, 1335
Wilner, D. J., Reid, M. J., & Menten, K. M. 1999, ApJ, 513, 775
Windhorst, R. A., Miley, G. K., Owen, F. N., Kron, R. G., & Koo, D. C. 1985, ApJ, 289, 494
Wright, E. L., Eisenhardt, P. R. M., Mainzer, A. K., et al. 2010, AJ, 140, 1868
Wu, Y. W., Sato, M., Reid, M. J., et al. 2014, A&A, 566, A17
Yang, A. Y., Thompson, M. A., Tian, W. W., et al. 2019, MNRAS, 482, 2681
Yang, A. Y., Urquhart, J. S., Thompson, M. A., et al. 2021, A&A, 645, A110

Appendix A: Low signal-to-noise ratio radio sources

We identified 1578 radio sources that have a S/N between 5 and 7σ. In Table A.1 we list these sources with the measured basic properties observed in the radio maps.

Table A.1. Catalog of sources with S/N in the range between 5 to 7σ.

GLOSTAR name	ℓ	b	S/N	$S_{\rm peak}$	$\sigma_{S_{\rm peak}}$	$S_{\rm int}$	$\sigma_{S_{\rm int}}$	SIMBAD	D-conf.
	(°)	(°)		(mJy beam^{-1})		(mJy)		class	name
(1)	(2)	(3)	(4)	(5)	(6)	(7)	(8)	(9)	(10)
G028.0142+00.5778	28.01418	+0.57782	5.2	0.20	0.07	0.34	0.07	...	...
G028.0181+01.0039	28.01809	+1.00390	5.1	0.34	0.11	0.54	0.11	...	...
G028.0210+00.8308	28.02103	+0.83082	5.3	0.18	0.07	0.37	0.07	...	...
G028.0217+00.3191	28.02170	+0.31913	5.1	0.18	0.07	0.35	0.07	...	...
G028.0252−00.1458	28.02525	−0.14580	5.4	0.20	0.07	0.35	0.07	...	...
G028.0288+00.7505	28.02882	+0.75047	5.0	0.20	0.07	0.33	0.07	...	...
G028.0295+00.1057	28.02948	+0.10573	5.3	0.20	0.07	0.39	0.08	...	...
G028.0431+00.5314	28.04308	+0.53136	5.8	0.32	0.07	0.39	0.07	...	...
G028.0514−00.7841	28.05139	−0.78409	5.1	0.18	0.06	0.32	0.07	...	...
G028.0573+00.2387	28.05733	+0.23871	5.8	0.21	0.07	0.40	0.07	...	...
G028.0576+00.8389	28.05756	+0.83895	5.1	0.16	0.07	0.33	0.07	...	...
G028.0790−00.7437	28.07896	−0.74374	5.0	0.18	0.06	0.32	0.07	...	...
G028.0894+00.5602	28.08940	+0.56018	5.3	0.20	0.07	0.36	0.07	...	...
G028.0980−00.7435	28.09799	−0.74353	6.7	0.25	0.06	0.42	0.07	...	...
G028.1029+00.8823	28.10291	+0.88229	5.2	0.19	0.07	0.33	0.07	...	...
G028.1052+00.3603	28.10524	+0.36031	5.3	0.18	0.07	0.35	0.07	...	...

Notes: Only a small portion of the data is provided here. The full table is available in electronic form at the CDS via anonymous ftp to cdsarc.u-strasbg.fr (130.79.125.5) or via http://cdsweb.u-strasbg.fr/cgi-bin/qcat?J/A&A/ and through the dedicated GLOSTAR webpage https://glostar.mpifr-bonn.mpg.de/glostar/.

Appendix B: Sample of the multiwavelength classification

We searched the prominent IR surveys to perform a visual inspection in the position of the highly reliable radio sources. Using this visual inspection, we performed the classification described in Sect. 3.8. In Figs. B.1, B.2, B.3, and B.4, we show examples of the images used for the classification as H II region candidates, radio stars, PNe, and EgCs, respectively. In addition to the images of the surveys described in Sect. 3.8, we included the images of the 24-μm emission from the Multiband Imaging Photometer *Spitzer* Galactic Plane Survey (MIPSGAL Carey et al. 2009).

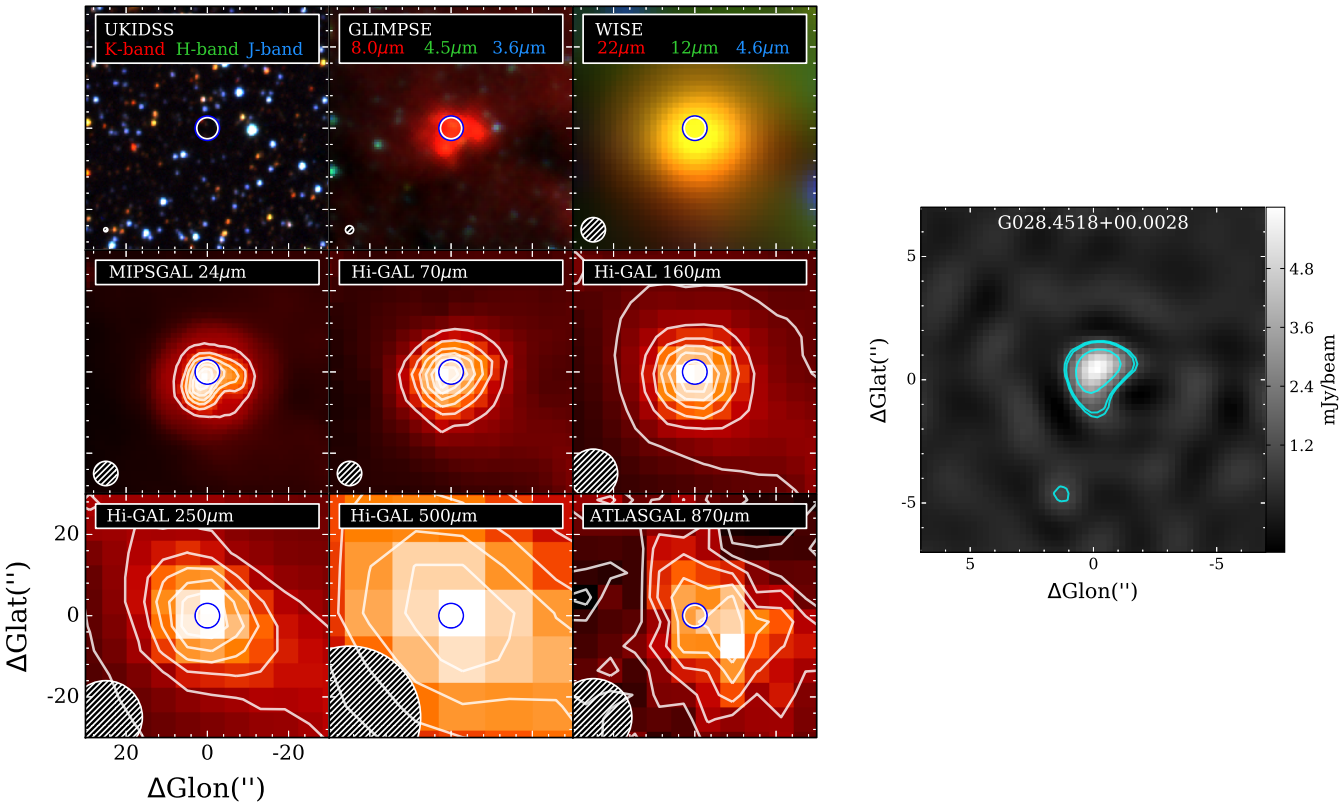

Fig. B.1. Example of a radio source classified as HII region. *Left:* Panels from the top left to the bottom right are RGB image of UKIDSS three observed bands, RGB image of GLIMPSE three observed bands, WISE 12 μm, Hi-GAL 70 μm, Hi-GAL 160 μm, Hi-GAL 250 μm, Hi-GAL 500 μm, and ATLASGAL 870 μm. *Right:* Radio source detected in the GLOSTAR B-configuration image.

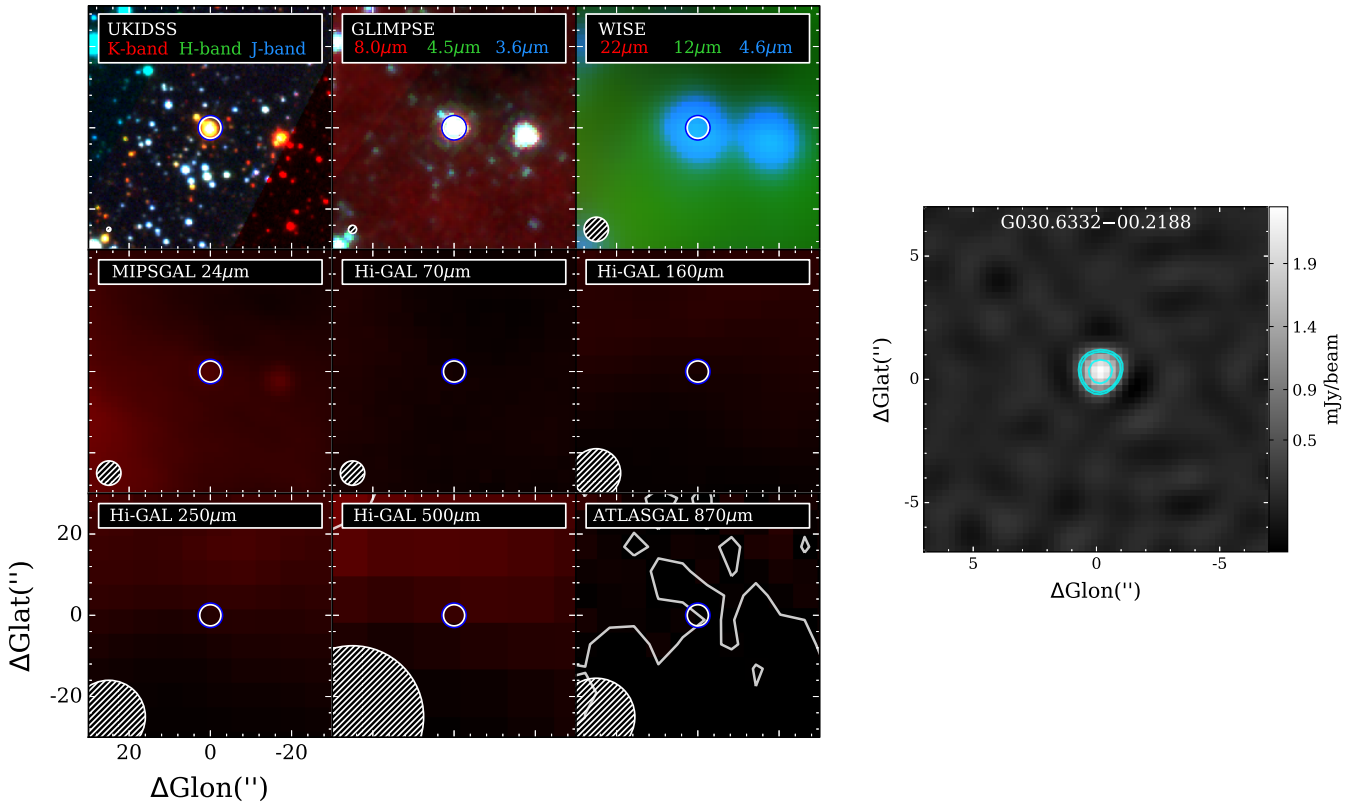

Fig. B.2. Same as for Fig. B.1, but for a radio source classified as radio star.

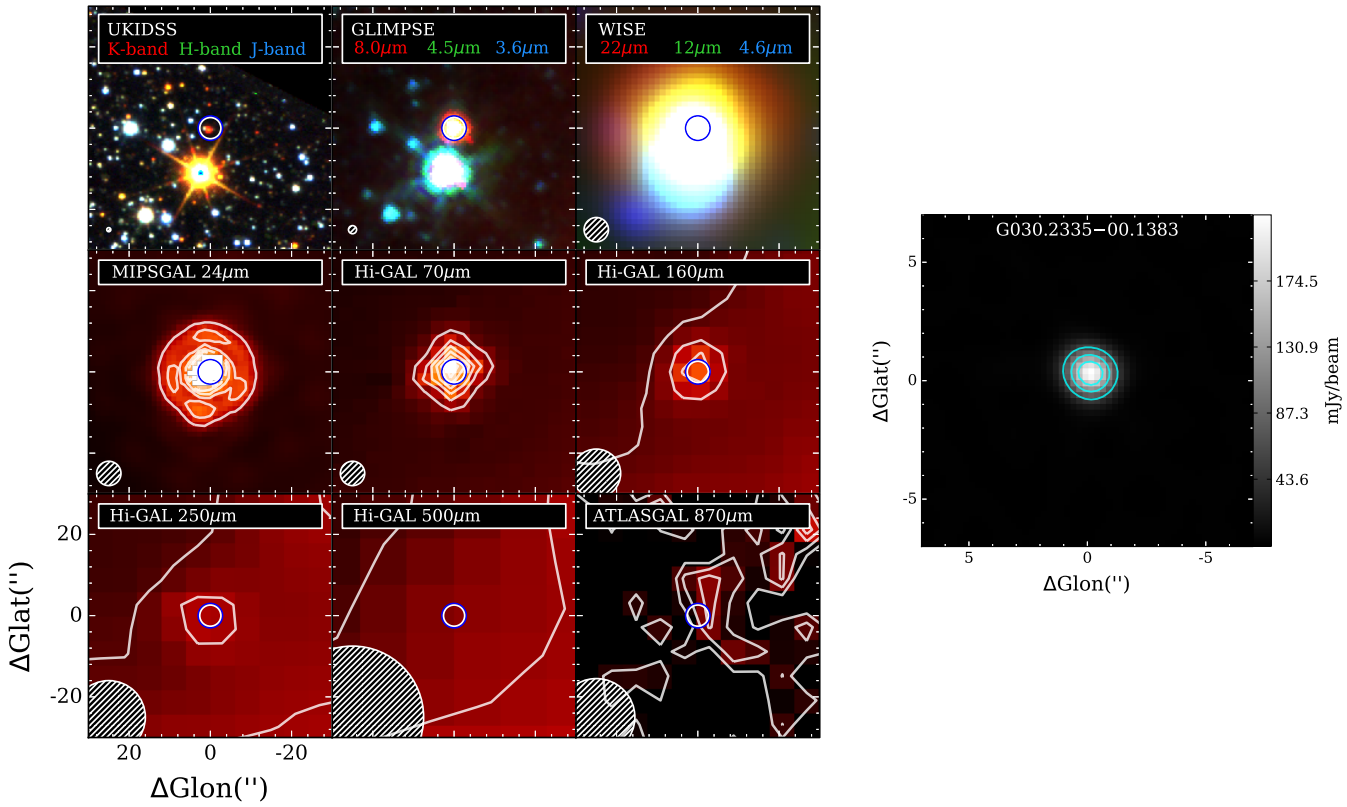

Fig. B.3. Same as for Fig. B.1, but for a radio source classified as PN.

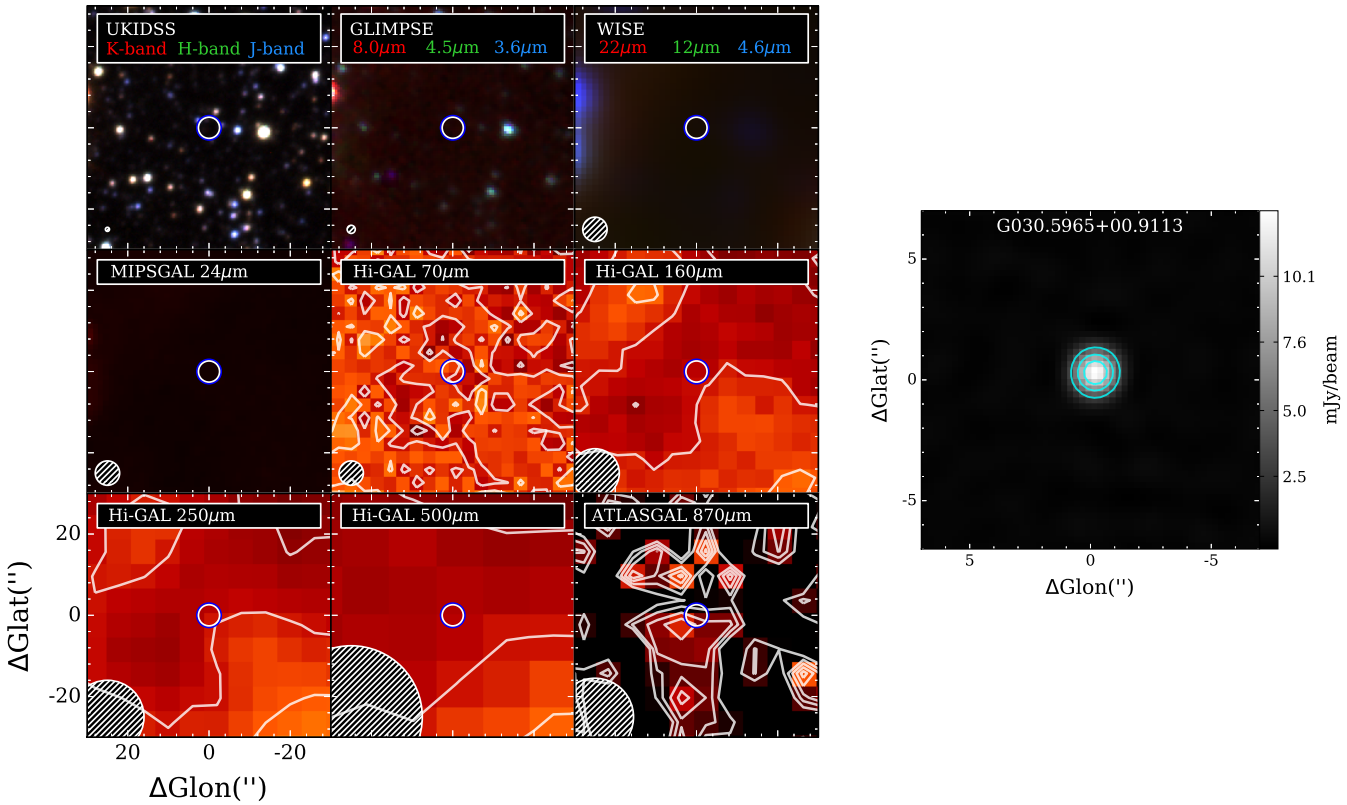

Fig. B.4. Same as for Fig. B.1, but for a radio source classified as EgC.

Appendix C: MIR emission around identified HII region candidates

In this appendix, we present a series of images to show the MIR emission as seen by the GLIMPSE survey centered at the position of the identified HII region candidates. The images are boxes with a size of 90″ × 90″, and the false colors are defined to be red, green, and blue for 8.0, 4.5, and 3.6 μm, respectively.

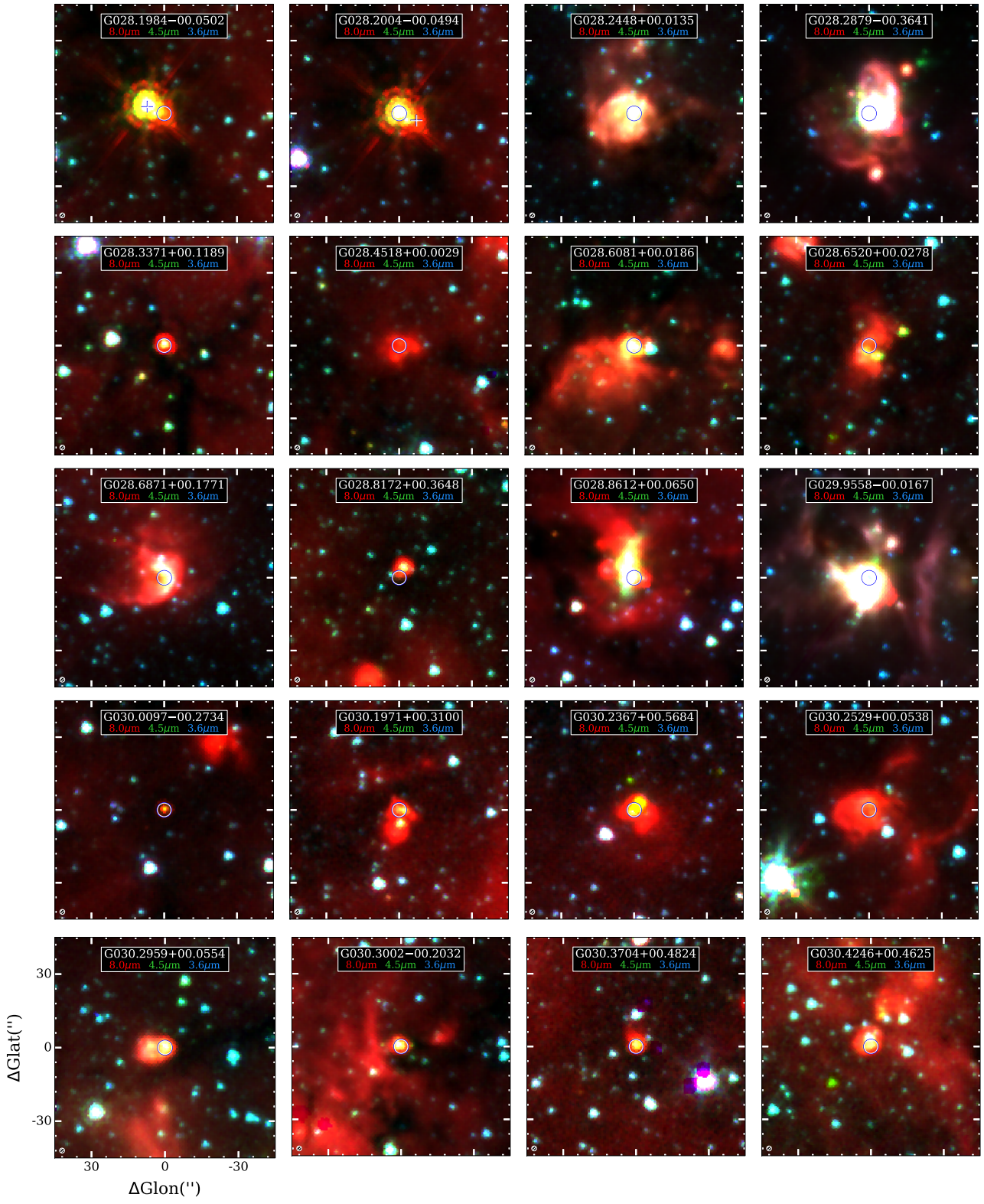

Fig. C.1. Three-color GLIMPSE images at the position of the HII region candidates identified in the GLOSTAR B-configuration images. In the case of the fragmented HII regions, listed in Table 2, the position of additional fragment sources are shown with lime-white crosses.

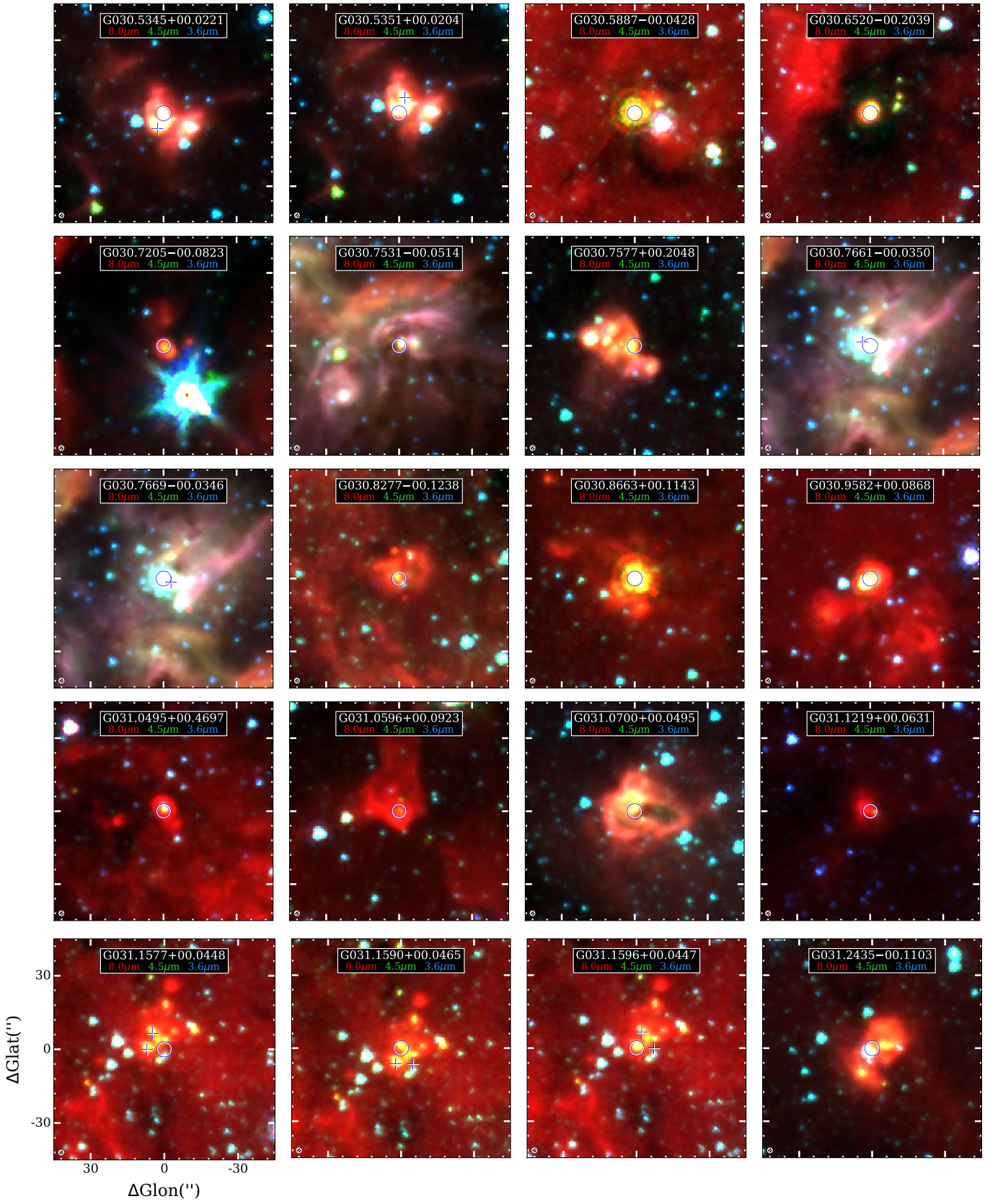

Fig. C.1. Continue.

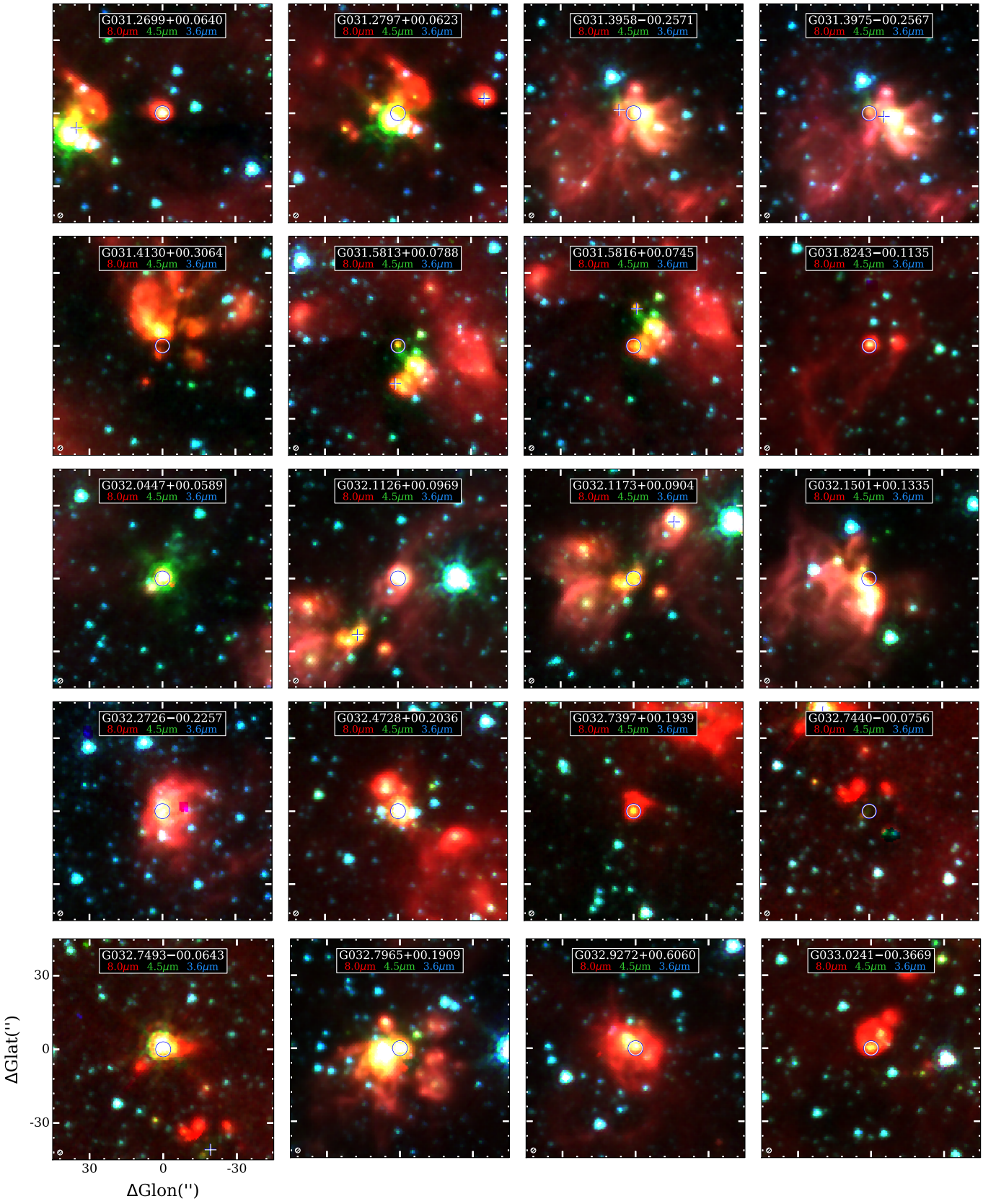

Fig. C.1. Continue.

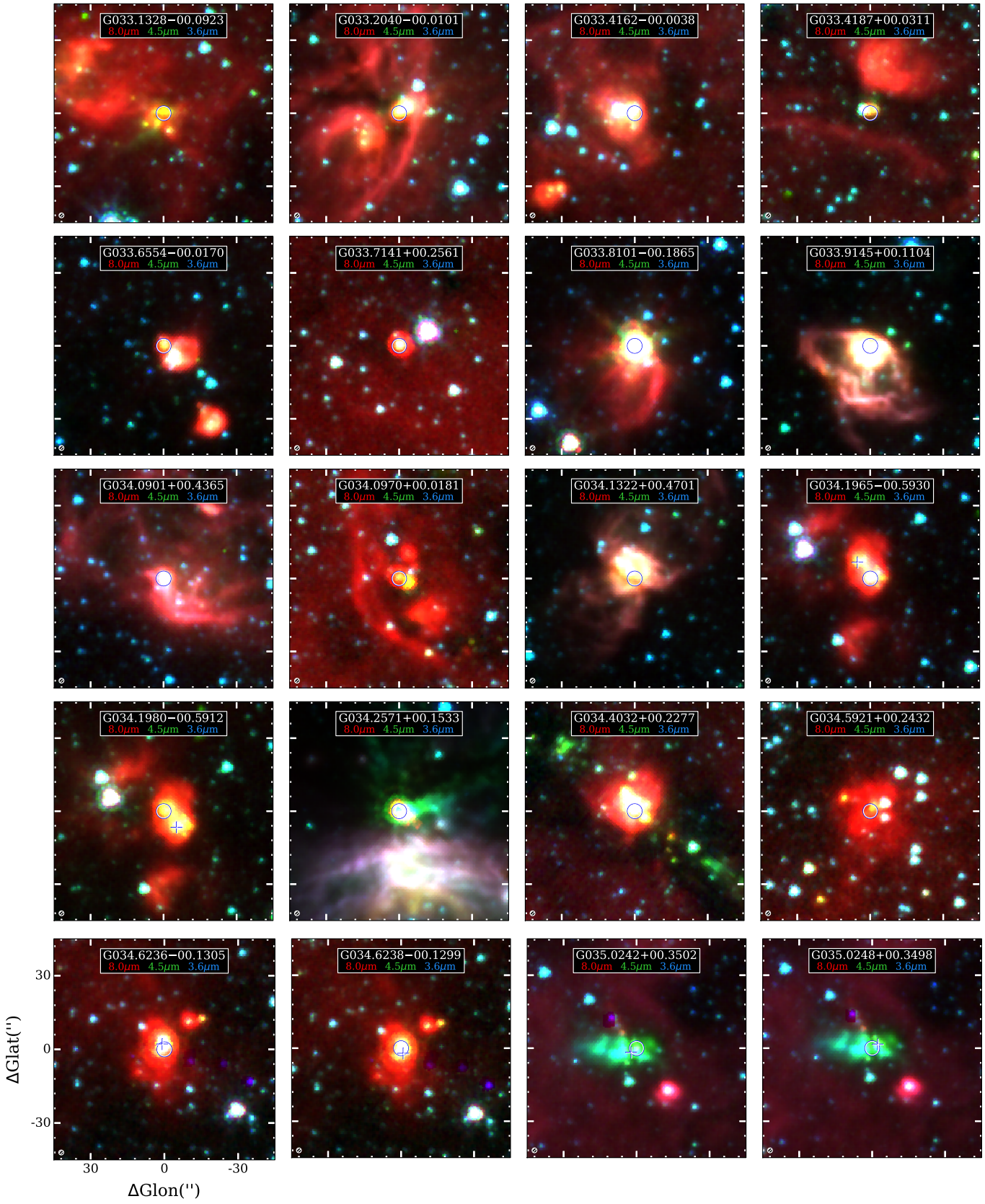

Fig. C.1. Continue.

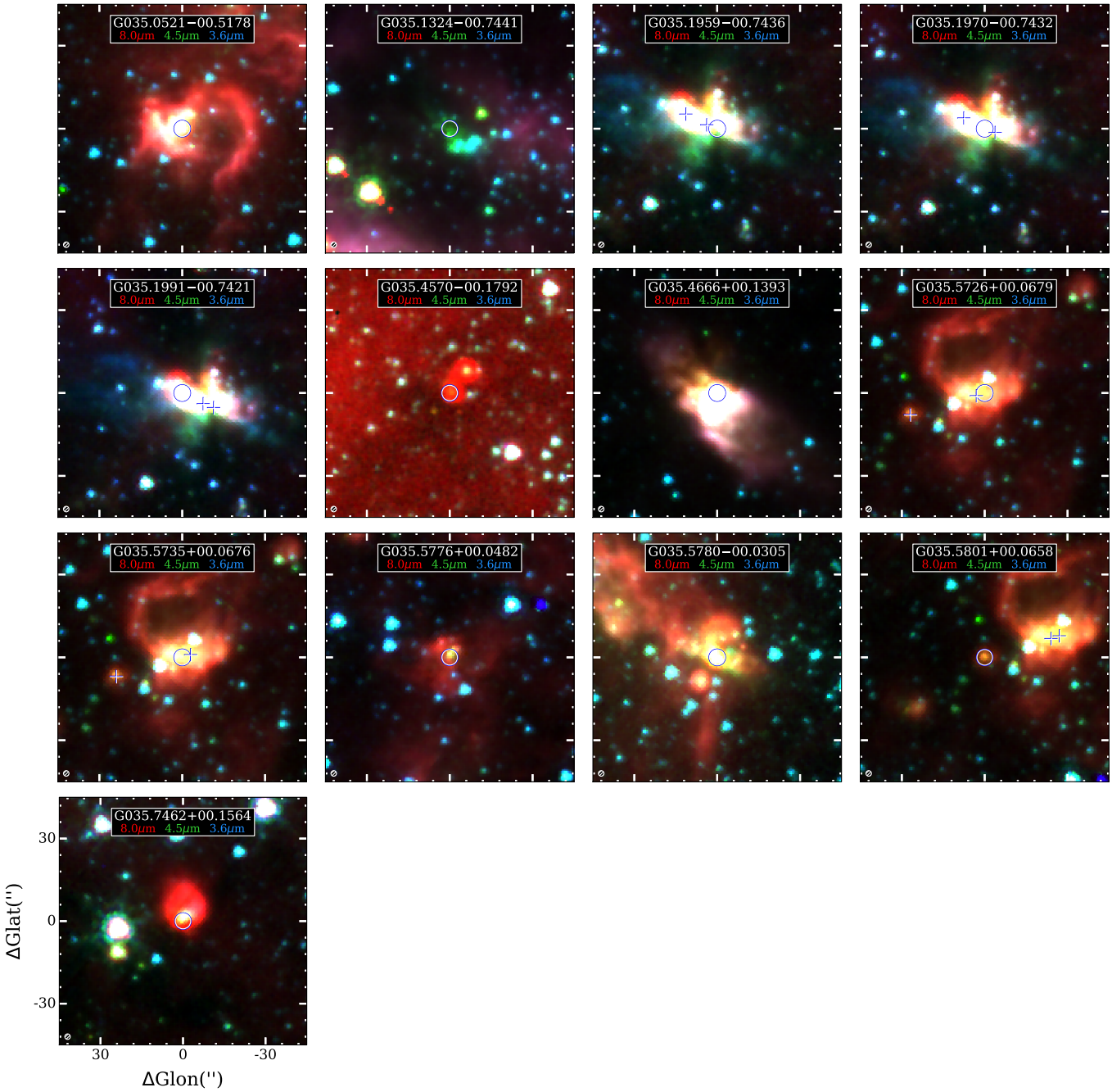

Fig. C.1. Continue.